IMAGING AND MEASUREMENT OF THE POROELASTIC BEHAVIOR OF

MATERIALS USING NEW ULTRASOUND ELASTOGRAPHY TECHNIQUES

A Dissertation

by

ANUJ CHAUDHRY

Submitted to the Office of Graduate and Professional Studies of
Texas A&M University
in partial fulfillment of the requirements for the degree of

DOCTOR OF PHILOSOPHY

| | |
|---|---|
| Chair of Committee, | Raffaella Righetti |
| Committee Members, | Steven M. Wright |
| | J. N. Reddy |
| | Jun Kameoka |
| Head of Department, | Miroslav M. Begovic |

December 2016

Major Subject: Electrical Engineering

# ABSTRACT

Ultrasound elastography (USE) is a well-established technique used to non-invasively map tissue stiffness.  More recently, a novel branch of USE, called poroelastography, has been proposed, which aims at estimating the poroelastic response of a tissue. The hypothesis of poroelastography is that underlying pathology, such as cancer, alters the fluid transport mechanisms in the tissue, which alters its poroelastic response. Poroelastography techniques estimate the temporal behavior of axial strain and effective Poisson's ratio (EPR) of a poroelastic media under compression. While these methods have been successfully proven to estimate the poroelastic response of poroelastic media and tissues, there are some major limitations which need to be addressed. There is a lack of tissue mimicking poroelastic phantoms with tunable poroelastic properties. Also, while US poroelastography techniques aim to estimate the temporal behavior of EPR, the estimation of the EPR using USE is challenging due to known image quality limitations of lateral strain elastography techniques. Also, the relationship between the spatio-temporal behavior of interstitial fluid pressure (IFP), axial strain and EPR is currently not known. IFP is an important parameter, which is known to help in the diagnosis and characterization of soft tissue cancers. In this dissertation, I attempt to solve some of these current issues in the field of ultrasound poroelastography imaging, taking the field one step forward.

In this work I investigated the use of polyacrylamide gel for creating new class of phantoms for poroelastography. Results of the study indicate that by using

polyacrylamide gel, tissue mimicking poroelastic phantoms with controlled fluid flow can be generated. This new class of phantom material can be used to conceptualize and validate techniques in poroelastography and for temporal ultrasound elastography imaging in general.  For reliable estimation of EPR, I proposed a new US poroelastography technique which uses two ultrasound transducers. By using a simulation module, image quality from this new technique was statistically compared from previously used methods. The feasibility to experimentally estimate EPR using two-transducers was also demonstrated. The results indicate that the two-transducer poroelastography technique has superior image quality than the existing methods.  In this study, I also studied the spatio-temporal behavior of axial strain, EPR and IFP with change in interstitial permeability. A 2D poroelastic finite element model was used, followed by an ultrasound simulation algorithm. The temporal behavior was estimated by finding the time constant of the temporal curves. Results of the analysis indicate that increased IFP creates a new contrast mechanism in both the axial strain and EPR elastograms. Also, the spatio-temporal patterns of IFP are closely related to that of the EPR and, hence,a reliable estimation of EPR may aid in a non-invasive assessment of underlying IFP.

DEDICATIONS

To my parents, sisters and family for their unconditional financial and emotional support during my PhD.

To my wife Sandala, for her patience and support through the ups and downs of graduate life.

And finally, to all my roommates, and friends, for constantly asking, "when are you going to graduate?"

# ACKNOWLEDGEMENTS

I would like to thank my committee chair, Dr. Righetti, for her vision, guidance and support through the last 8 years of my association with her. Personally and professionally, I have learned a lot from her. I would also like to thank my committee members, Dr. Reddy, Dr. Wright, and Dr. Kameoka, for their guidance and support throughout the course of this research.

I would also like to thank my colleagues, Biren, Sanjay, Shafeeq, Songyuan,  Xu,  Kuan, , Sthiti and Raghu, Tauhid, for their support and help during my stay at the ultrasound imaging laboratory.

Special thanks to Dr. JN Reddy's lab, for guidance and collaboration through this work. I would especially like to thank Dr. Ginu and Namhee, for their patience in answering my questions.

I would also like to thank Dr. Ennio's lab at Houston Methodist, for their collaboration. Special thanks to Joe, Jeff, Iman and Fernando, for their help on projects conducted at Methodist Research.

I would also like to thank Dr. Thomas Krouskop, for the many scientific discussions I had with him and for his insights on this work.

Special thanks to Rohit Kongari (Chiru) and Dr. Giridhar Sekar (Giri), for helping me understand the biochemistry concepts used in this dissertation.

# NOMENCLATURE

EPR            Effective Poisson's Ratio

TT             Two-Transducer

IFP            Interstitial Fluid Pressure

t              Time

s              Seconds

US             Ultrasound

TABLE OF CONTENTS

LIST OF FIGURES

LIST OF TABLES

# 1. INTRODUCTION

In this section I present some of the relevant concepts of poroelastic materials in relationship to human tissues. I also discuss the background of ultrasound poroelastography techniques in current literature.

## Background on poroelastic materials

Biot's work from 1935 to 1941 (Biot 1935, Biot 1941) is considered the basics for the theory of linear poroelasticity. Bowen (1982) and Mow et al. (1980) proposed the use of mixture theory which have developed from the consolidation theory and have been widely used to model the poroelastic behavior of tissues. According to these theories, a poroelastic material is defined as a material that contains more than one phases in which at least one the phases is solid (Mow, et al. 1984). For human tissues we can restrict the number of phases to two- a solid phase containing the interstitial matrix and the liquid phase containing the interstitial fluid which can move with respect to the solid phase (Armstrong, et al. 1984, Torzilli and Mow 1976) .

For a poroelastic material under uni-axial compression the temporal behavior of the axial and lateral strains is mathematically dependent on the underlying pressure fields(Armstrong, et al. 1984). Under uniaxial loading three temporal stages can be observed: 1) instantaneously after loading, the material behaves like an incompressible solid. The stress is fully supported by the fluid phase, which increases the pore pressure; 2) the stress is then partially transferred to the solid matrix, and fluid begins to exude causing a decrease in volume and EPR. During this transition time, the pore pressure

also decays as the solid matrix deforms both in the axial and lateral directions 3) when the equilibrium condition is reached, fluid flow ceases and the pore pressure drops to zero. The rates at which the axial strain and EPR reach their equilibrium value depend upon the ease at which the interstitial fluid flows which in turn depends upon the relaxation of the underlying pressure fields (Leiderman, et al. 2006). For one-dimensional geometry, a poroelastic material may be completely characterized by three parameters (Armstrong et al 1984):   the Young's modulus of the solid matrix; the Poisson's ratio of the solid matrix and the permeability of the poroelastic medium.

In the past, several tissues have been modeled as poroelastic materials because of their relatively high fluid content and fluid mobility (Mow, et al. 1984, Mridha and Odman 1986, Torzilli and Mow 1976). These include: cartilage, cornea, tendons, ligaments, brain, and breast and lymphedematous tissues (Fatt 1968, Jurvelin, et al. 1997, Mow, et al. 1984, Van Houten, et al. 2003). Most tumors are known to possess fluid transport properties that are different from normal tissue (Jain 1994, Lunt, et al. 2008, Milosevic, et al. 2001, Milosevic, et al. 2008, Netti, et al. 1995, Stapleton and Milosevic 2013). Malignant tumors have often significantly lower compressibility with respect to normal tissue, presumably due to tissue fibrosis or a collapse of the interstitial matrix(Leunig, et al. 1992). This decreased permeability is a major cause for elevated interstitial fluid pressure (IFP) (Boucher, et al. 1990), which is a limiting factor in drug delivery therapies (Boucher, et al. 1990). In addition, several cancer treatments are known to modify the permeability of tumors (Park 2002). Lymphedema is a common consequence to cancer and cancer treatments (Petrek, et al. 2001). This condition manifests as an

2

abnormal accumulation of interstitial fluid due to damage of the lymphatic system(Szuba and Rockson 1997). Previous studies in this field have shown that lymphedematous tissues may be modeled as poroelastic tissues (Raffaella, et al. 2007, Raffaella, et al. 2007). These studies have also suggested that poroelastography may have significant potentials for detecting and, possibly, staging this condition.

## Background on poroelastography

Ultrasound elastography is a collection of techniques which are used to map tissue stiffness by application of a force (Bercoff, et al. 2004, Nightingale, et al. 2001, Ophir, et al. 1991, Sandrin, et al. 2003). The usefulness of these techniques in medicine is due to the fact that underlying pathology alters tissue structure and composition changing its stiffness.  Many malignant changes like cancers of the breast or prostate appear as lesions of higher stiffness (Itoh, et al. 2006, Sarvazyan, et al. 2011). In classical quasi-static elastography local tissue displacements are mapped on application of a small external compression by using cross correlation techniques on digitized ultrasound RF signals (Cespedes, et al. 1993). The local strains are then displayed as the gradient of the computed displacements. The resulting image is called an elastogram (Ophir, et al. 1996).

More recently many new techniques have evolved from quasi-static elastography which aim at estimating new mechanical parameters about the tissue (Konofagou, et al. 2001, Thitaikumar, et al. 2007). Poroelastography is one such branch of ultrasound elastography that aims at imaging the temporal response of tissues under

3

compression(Righetti, et al. 2004). The hypothesis of poroelastography is that the altered fluid transport mechanisms caused due to change in tissue structure alters their poroelastic response (Chaudhry, et al. 2013, Konofagou, et al. 2001). This change is response can be assessed by estimating the temporal behavior of axial strains and 'effective' Poisson's ratio (EPR) (Righetti, et al. 2005, Righetti, et al. 2007).

A poroelastogram is defined as a time sequence of axial strain or EPR elastograms obtained from the poroelastic material under compression. The 'effective' Poisson's ratio (EPR) is calculated as the division of the estimated lateral strain by the estimated axial strain from elastographic experiments. It is called 'effective' because it is not the true Poisson's ratio of the material and depends on a number of factors including Young's modulus of the solid matrix, permeability and viscosity of fluid phase, Poisson's ratio of the solid matrix and fluid content. The EPR of a poroelastic material indicates its compressibility which loosely means its ability to change volume under compression.

(Konofagou, et al. 2001) reported the first simulation work on poroelastography, which showed the feasibility of mapping local EPR in uniform homogeneous poroelastic media. This work was later validated in phantoms and ex-vivo samples by (Righetti, et al. 2004) which showed that elastography can be used to monitor time dependent changes in porous media. The effect of interstitial fluid flow on the spatio-temporal behavior of strain fields have been studied through analytical models and validated experimentally (Berry, et al. 2006, Berry, et al. 2006, Leiderman, et al. 2006). Many

studies have proposed to compute temporal elastographic parameters from axial strain and EPR temporal curves obtained from poroelastic media under compression (Nair, et al. 2011, Righetti, et al. 2005, Righetti, et al. 2007). To quantify the performance limitation of poroelastography technique image quality parameters such as signal-to-noise ratio, contrast-to-noise ratio and resolution have also been analyzed (Raffaella, et al. 2007, Righetti, et al. 2007).

Most of the experimental ultrasound poroelastography studies retrievable in the literature deal with the use of axial strain estimation techniques. The EPR of a poroelastic tissue is related to the effective compressibility of the material, which in itself depends on the ability of the material to change volume under load and allow fluid movement (Wang 2000). While most soft tissues are typically modelled as "incompressible" linearly elastic solids (i.e., with a Poisson's ratio close to 0.5) – an assumption that is typically valid only under quasi-static compression - a poroelastic material is by definition compressible in order to allow fluid translocation (Sarron, et al. 2000). Estimation of the EPR using ultrasound elastography is challenging, due to known image quality limitations of lateral strain elastography techniques (Kallel, et al. 1997). However, knowledge of this parameter is in general important to correctly interpret the observed tissue temporal changes, and to confirm that these changes are indeed caused by underlying poroelastic effects rather than, for instance, viscoelastic effects, which typically may not involve changes in volume. Additionally, EPR is related to the tissue's compressibility, a parameter of known diagnostic value and may provide a means to locally map the underlying IFP contrast of the tissue. The image quality of

EPR elastogram is limited by of the poor quality of standard lateral strain elastography (Kallel, et al. 1997). To improve the quality of lateral strain elastography and EPR, some studies have implemented advanced filtering techniques combined with spatial and temporal averaging (Raffaella, et al. 2007, Righetti, et al. 2005). However, experimentally averaging is not just difficult to implement but is highly time consuming making it extremely difficult to implement for clinical applications.

Poroelastography studies aim at observing the fluid flow behavior of poroelastic media under compression. Tofu has been shown to possess acoustic and mechanical properties reasonably close to that of soft tissue(Wu 2001). It also has high fluid content which can flow with respect to the solid structure on compression, allowing the material to change volume on compression. Due to these reasons, many poroelastography and temporal elastography studies in general have used tofu as a phantom for validating the theoretical and simulation concepts (Berry, et al. 2006, Nair and Righetti 2015, Righetti, et al. 2005, Wu 2001). Although being an excellent tool for proving preliminary poroelastography concepts, the use of tofu as a phantom material has some limitations. Being a commercial product tofu does not come with known mechanical parameters and the poroelastic properties are not consistent between samples.  Also the fluid flow and poroelastic properties of tofu cannot be altered to make precise phantoms of known fluid flow and stiffness.  A new phantom material with acoustic and mechanical properties close to that of soft tissue and tunable poroelastic behavior will help the field of poroelastography move forward.

Interstitial fluid pressure (IFP) is a parameter of high relevance especially for soft tissue tumors. IFP or simply pore pressure is the pressure experienced by the tissue interstitium due to leaky microvasculature and weak lymphatic drainage. Many elastography studies have aimed to analyze the detectability of these tumors based on their stiffness (Ginat, et al. 2009, Hiltawsky, et al. 2001). The results are often interpreted based on modelling the tumor as linearly elastic incompressible solid (Kallel and Bertrand 1996). Under these assumptions a contrast in the axial strain elastograms is interpreted as a contrast in underlying elastic modulus of the tissue (Doyley 2012). The effect of elevated IFP on US elastography technique is largely unknown. Knowledge of the effect of this parameter may aid in future interpretations of application of elastography technique to tumors, especially for cases with known elevated IFP.

For a poroelastic material under uni-axial compression, the temporal response is governed by fluid translocation mechanisms which in turn depends on local pressure gradients (Armstrong, et al. 1984). Upon compression the material changes volume due to exudation of fluid resulting is pressure relaxation, which also causes the EPR of the material reduces from about 0.5 (nearly incompressible) to its equilibrium value. However the relationship between poroelastography parameters and underlying fluid pressure (IFP) is not known. Also to my knowledge, no ultrasound imaging modality can be used to non-invasively map changes in the IFP. The only non-invasive modality found in recent literature that can provide an indicator of IFP uses dynamic contrast MRI to measure velocity of fluid flow on tumor surface (Hassid, et al. 2006, Hompland, et al. 2012). Investigation of relationship between the temporal behavior of EPR and IFP may

encourage future research in the use of US poroelastography techniques for non-invasive assessment of underlying fluid pressure.

## Hypothesis

I hypothesize that new ultrasound elastography techniques can be used to assess effective Poisson's ratio of poroelastic materials with high contrast-to-noise ratio and accuracy. I further hypothesize that images and measurements of the local effective Poisson's ratio of poroelastic tissues obtained via ultrasound elastography techniques are correlated with changes of the underlying tissue's interstitial fluid pressure (IFP) distribution. The following aims are included in this investigation:

1)      Develop and test a new class of poroelastic phantoms with tunable echogenicity and poroelastic properties.

2)      Design and test a new ultrasound elastography method to measure the Effective Poisson's Ratio (EPR) in poroelastic tissues with high signal-to-noise ratio, contrast-to-noise ratio and accuracy

3)      Investigate the relationship between EPR and underlying pore pressure in poroelastic phantoms and tissues.

# 2. A NEW CLASS OF PHANTOM MATERIALS FOR POROELASTOGRAPHY IMAGING TECHNIQUES[*]

## Introduction

Ultrasound elastography is an established imaging modality used to map the local strains of a soft tissue under quasi-static compression (Ophir, et al. 1999, Ophir, et al. 1991). The technique has been used to image tumors on the basis of their elastic properties in vivo (Hiltawsky, et al. 2001, Lorenz, et al. 2000, Zhi, et al. 2007). Poroelastography is a branch of ultrasound elasticity imaging that deals with tissues that can be modelled as porous material such as breast, brain, prostate, liver, cartilage, muscle etc. (Konofagou, et al. 2001, Leiderman, et al. 2006, Nair, et al. 2014, Raffaella, et al. 2007, Raffaella, et al. 2007, Righetti, et al. 2004). The basis at the development of poroelastography is that fluid content and transport mechanisms within a tissue can be altered by pathological conditions (Berry, et al. 2006, Konofagou, et al. 2001, Leiderman, et al. 2006, Raffaella, et al. 2007). For example, most tumors are known to possess fluid transport properties that are different from normal tissue (Jain 1994, Lunt, et al. 2008, Milosevic, et al. 2001, Milosevic, et al. 2008, Netti, et al. 1995, Stapleton and Milosevic 2013). These changes can be estimated by subjecting the tissue to a small compression and observing the time-dependent mechanical response (Nair, et al. 2011, Righetti, et al. 2011). Assessment of

---

[*] Reprinted with permission from "A new class of phantom materials for poroelastography imaging techniques" by "Chaudhry A, Yazdi IK, Kongari R, Tasciotti E, Righetti R", ultrasound in medicine and biology, Vol 42, Issue 5, pg 1230-1238. Copyright (2016) by Elseivier.

this temporal response may aid in the diagnosis and treatment of many diseases such as lymphedema and cancers (Mridha and Odman 1986, Qiu, et al. 2008).

Poroelastography techniques aim at imaging the axial strain distribution and/or the effective Poisson's ratio (EPR) distribution and their temporal evolutions experienced by a tissue under sustained compression (Chaudhry, et al. 2013, Nair, et al. 2014, Raffaella, et al. 2007). During sustained loading, solid matrix deformation and fluid translocation occur in the poroelastic tissue due to established pressure gradients (Detournay and Cheng 1993, Wang 2000), causing changes in the spatial and temporal distribution of the axial strain and the EPR experienced by the tissue (Chaudhry, et al. 2013, Righetti, et al. 2004).

One of the major challenges in the field of temporal elastographic imaging has been the lack of controlled phantoms that could be used to help validate the experimental results in a variety of conditions. Gelatin-based phantoms have been the most common choice of materials for controlled experimental elastographic studies. Gelatin-based phantoms are typically very simplistic and do not exhibit significant temporal behavior. In fact, even though they contain a relatively large amount of water, this water is bounded and not free to move during compression. More recently, tofu has been proposed for poroelastographic controlled experiments (Nair, et al. 2014, Nair, et al. 2011, Righetti, et al. 2005). It has been shown that tofu possesses mechanical and ultrasonic properties similar to those of soft tissues, is inexpensive and easily accessible(Wu 2001). However, there is a large variability between different brands and types of tofu. In addition, being a

commercial product, it is not possible to alter its mechanical properties to investigate more realistic experimental situations. The construction of complex in-homogenous elastographic phantoms using tofu materials, for e.g. fully connected multi-inclusion or multi-layer phantoms, is very challenging and hard to standardize. As a result, up to now, tofu has been almost exclusively used for controlled experiments involving homogenous and simplistic phantoms. In this study, we propose the use of polyacrylamide gel as a new tissue mimicking phantom for poroelastography studies. This material can be used to construct homogeneous and non-homogeneous phantoms that are easy to reproduce and exhibit a range of tunable mechanical and temporal properties.

Polyacrylamide gels are commonly used in the electrophoresis to separate protein, DNA and other molecules (Blattler, et al. 1972, Chrambach and Rodbard 1971, Raymond and Wang 1960, Tombs 1965). These gels are prepared by free radical polymerization of acrylamide (T) and a crosslinker such as bis-acrylamide (C). Polymerization is initiated by ammonium persulfate (APS) with tetramethylethylenediamine (TEMED) as the catalyst (Chrambach and Rodbard 1971, Holmes and Stellwagen 1991). The major advantage of using polyacrylamide gel for poroelastic applications is that their pore size and hence the fluid mobility can be altered by either changing the percentage of acrylamide and/or the crosslinker i.e. bis-acrylamide (Blattler, et al. 1972, Chrambach and Rodbard 1971, Holmes and Stellwagen 1991, Raymond and Wang 1960, Tombs 1965). Higher concentrations of %T generate phantoms with smaller pore size but increases the stiffness of the gel (Boudou, et al. 2006, Tse and Engler 2010). Higher %C

11

also reduces the pore size with minimal changes in stiffness. Smallest pore sizes were found to be at 5% and 10%C (Holmes and Stellwagen 1991). Polyacrylamide gels on their own do not possess any echogenicity and hence cannot be for ultrasound applications (Kawabata, et al. 2004). Agar has been used to provide echogenicity in commonly used gelatin-agar elastography phantoms (Hall, et al. 1997, Kallel, et al. 2001, Madsen, et al. 2005). A review of previous literature on the acoustic properties such as speed of sound, impedance and attenuation of polyacrylamide materials is reported in Table 1. These numbers are comparable to those of human soft tissues such as skin, breast, liver, kidney, muscle and also to that of the gelatin-agar phantoms traditionally used as a tissue mimicking material for quasi-static ultrasound elastography studies (Bamber and Hill 1979, Bamber 2007, Culjat, et al. 2010, Duck 2013, Hall, et al. 1997, Kallel, et al. 2001, Zell, et al. 2007). Due to their ultrasonic properties, polyacrylamide gels have also been used as a tissue mimicking phantom for focused ultrasound experiments (Choi, et al. 2013, Lafon, et al. 2001, Takegami, et al. 2004). Recent studies have also shown that temporal behavior of hydrated polyacrylamide gels are mainly related to their poroelastic properties (Galli, et al. 2009, Kalcioglu, et al. 2012). Their use in tissue engineering has increased interest in the last few years with studies showing their use for tissue filling in facial reconstruction (von Buelow, et al. 2005) and also as a replacement tissue for human cartilage (Li, et al. 2011).

| Reference | Speed of sound (m/s) | Density (gm/ml) | Impedance (MRayl) | Attenuation (dB/cm) | Method used |
|---|---|---|---|---|---|
| (Zell, et al. 2007) | 1580±50 | 1.09±0.009 | 1.73±0.08 | 0.7±0.1 | Insertion technique (Bamber 2007) |
| (Kharine, et al. 2003) | 1580±30 | 1.07±0.02 | 1.71±0.06 | 0.7±0.1 | Insertion technique (Bamber 2007) |
| (Prokop, et al. 2003) | 1546-1595 | 1.02 – 1.05 | 1.58 – 1.68 | 0.5±0.1 | Pulse transmission technique (Madsen and Frank 1999) |

Table 1: Acoustic properties and density of polyacrylamide gel.

**Materials and methods**

Acrylamide (40% v/v), bisacrylamide (2% v/v), ammonium persulfate (APS) and Tetramethylethylenediamine (TEMED) were used for the synthesis of the polyacrylamide gel. The reagents were purchased from Bio-rad laboratories, CA. Agar (Sigma-Aldrich, MO, USA) was used to add echogenicity in all phantoms (Kallel, et al. 2001).

The following procedure was used for preparing the polyacrylamide gels:

1)      5% Acrylamide (T) and the desired bis-acrylamide (C) solutions were mixed together with water in a container. To be consistent with existing

literature, the bis-acrylamide % was calculated as a ratio of bis to total

acrylamide solution given by

$$\%C = \frac{Cml}{Cml+Tml} * 100$$ ...................................................................... (1)

This concentration of bis-acrylamide was varied between 1% and 5% to make

poroelastic phantoms of different pore sizes.

2)      3% agar was added to all phantoms. Agar was mixed with water and

boiled separately till it dissolved. The mixture was degassed by stirring it for 5-

10 minutes and then allowed to cool down to about 40 ºC before mixing it with

the acrylamide solution.

3)      0.1% of APS and 0.1% of TEMED were used as initiator and catalyst

respectively to start the polymerization process.

4)      The resulting solution (500ml) was poured in a 6 X 6X 6 cm$^3$ mold and

aged overnight for the completion of polymerization.

Two kinds of phantoms were created, homogenous phantoms with varying %C and

phantoms with an inclusion. Four homogenous phantoms were created with 1%, 3%, 4%

and 5% C respectively. For the inclusion phantoms, a cylinder of 1.5 cm diameter was

created along one of the dimensions of the homogenous phantom. Polyacrylamide gel

solution of desired %C was then poured into this cylindrical mold to create the inclusion.

Three inclusion phantoms were made with chosen %C as detailed in Table 2. After the

phantoms were polymerized, they were submerged in water for 48 hours for complete

hydration. Selected results were compared to those obtained from a standard agar gelatin

phantom under the same testing conditions.  Agar gelatin phantoms are traditionally used

in quasi-static elastography. The gelatin phantom was prepared using 5% gelatin and 3% agar following the procedure given by (Kallel, et al. 2001).

| Case | a | b | c |
|---|---|---|---|
| %C background | 1 | 1 | 5 |
| %C inclusion | 5 | 3 | 1 |

Table 2: %C of inclusion and background of non-homogenous phantoms.

All elastography experiments were performed using our Ultrasonix RP (Richmond, Canada) linear array scanner, which operates at a 6.6 MHz center frequency, 50% fractional bandwidth with 1mm beamwidth (Nair, et al. 2014). The polyacrylamide phantoms were subjected to creep compression for 600 s with an acquisition frame rate of 1 frame/s.  A constant axial load of about 0.5 N was applied, which lead to 1-5% axial strains (Chaudhry, et al. 2013, Nair, et al. 2011). Axial and lateral displacements were calculated from two consecutive RF frames using cross-correlation techniques (Ophir, et al. 1996). The length of correlation window for both pre- and stretched post-compression RF signal was chosen as 1.5mm with 80% overlap between consecutive windows (Varghese and Ophir 1997). Axial and lateral strains were then computed using staggered strain estimation (SSE)(Srinivasan, et al. 2002). Axial strain time constant (TC) images were generated from the time series of axial strains using the Levenberg-Marquardt (LM) method (Nair, et al. 2011). To have a general idea of the image quality

of the proposed phantoms, commonly used elastographic image quality parameters namely the signal to noise ratio (SNRe) and the contrast to noise ratio (CNRe) were computed as previously documented in literature (Chaudhry, et al. 2013, Srinivasan, et al. 2003). Paired t-test analysis was performed to statistically analyze the estimated time constant measurements within a 30 pixel x 30 pixel ROI, which was chosen around the center of the image to avoid boundary condition effects.

In selected phantoms, the pore size and distribution were independently validated using Scanning Electron Microscopy (SEM)(Stokols and Tuszynski 2006, Tang, et al. 2004). For the SEM measurements, the polymerized gels were freeze-dried using a lyophilizer (Freezone 4.5, Labconco Corp., Kansas City, MO, USA) after freezing at −80°C overnight. Samples were mounted on aluminum stub using conductive adhesive tape and sputter coated with a 10 nm layer of platinum using a high resolution sputter coater high resolution sputter coater (Cressington 208HR, Cressington Scientific Instruments Ltd, UK). SEM was performed under high vacuum using a FEI Nova NanoSEM 230 (FEI Company, Hillsboro, Oregon, USA) at a voltage of 10 kV and spot size 3.0 under working distance of 5 mm (Murphy, et al. 2011). To have an idea of the overall stiffness of the gels, an Aixplorer®SuperSonic Imagine system (Aix-en-Provence, France) with a 3.5 MHz probe (SC6-1, SuperSonic Imagine) was used. The elastic modulus measurements were obtained in selected areas of the phantoms while the phantoms were fully hydrated and in equilibrium conditions (undrained, no fluid flow, no applied compression).

# Results

Figure 2.1 shows selected SEM images of homogenous polyacrylamide-agar phantoms

with different percentages of crosslinker (C). Note that the pore size decreases as the

concentration of C is increased from 1% to 5% keeping percentage of monomer (T) and

agar constant at 5% and 3% respectively. This change in pore size is similar to that

observed in (Holmes and Stellwagen 1991).
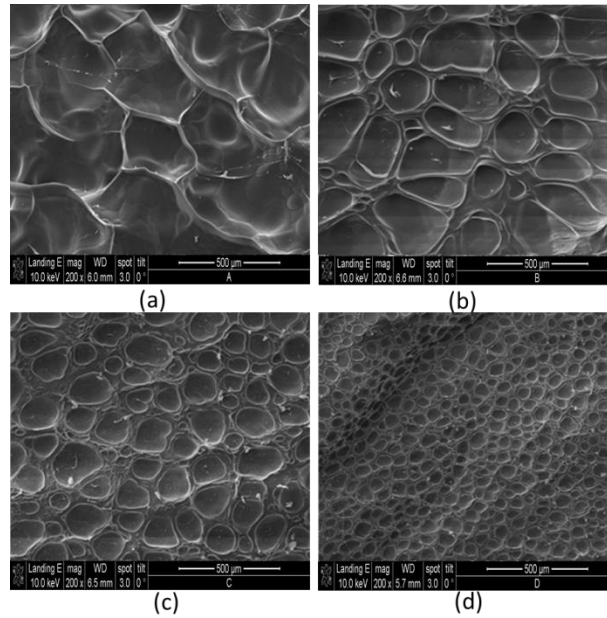


Figure 2.1: SEM images of homogeneous phantoms with (a) 1%C (b) 3%C (c) 4%C and
(d) 5% C.

Table 3 shows the estimated elastic modulus in selected phantoms. It can be seen that the

change in undrained elastic modulus is nominal with change in C, with increasing values

as the concentration of crosslinker increases. These measurements show that the elastic modulus of the proposed phantoms is within the range of human tissues and other phantom materials used for standard elastography measurements (Gao, et al. 1996, Ophir, et al. 1999).

| C % | 1 | 3 | 4 | 5 |
|---|---|---|---|---|
| Elastic Modulus (KPa) | 38±1.3 | 39±0.6 | 41±0.9 | 42±1.2 |

Table 3: Estimated elastic modulus of homogeneous polyacrylamide-agar gels with different %C.

Figure 2.2 shows axial strain poroelastograms obtained for the four different homogenous phantoms. Due to higher fluid mobility, the phantoms with larger pore size (top row) drain faster than the ones with smaller pore size. As a result the phantom with 1%C reaches equilibrium faster than the others while the one with 5%C is the one that takes the longest to reach equilibrium. Figure 2.3 shows the corresponding estimated mean time constants from the axial strain temporal data. It can be seen that the mean time constant increases with a decrease in pore size. . Figure 2.3 shows the corresponding estimated mean time constants from the axial strain temporal data. It can be seen that the mean time constant increases with a decrease in pore size.

18
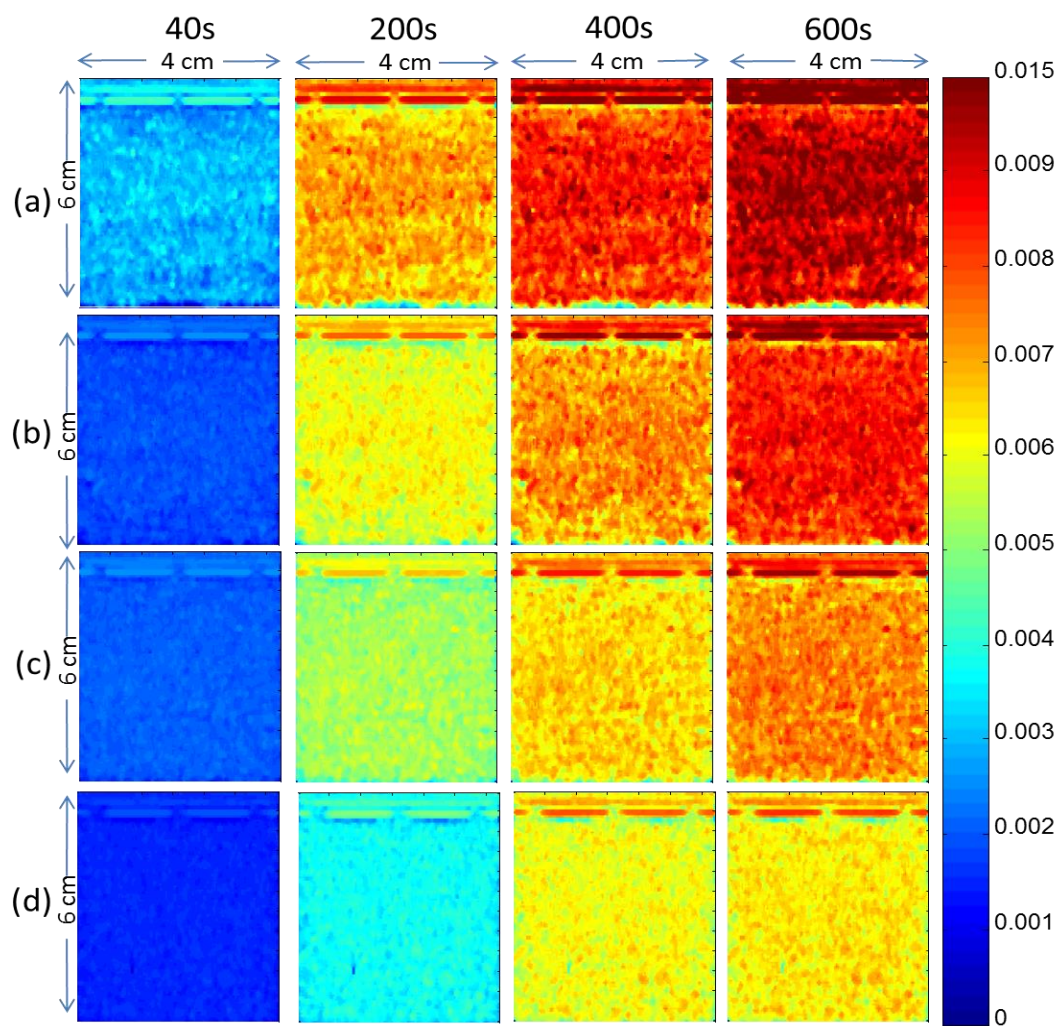
Figure 2.2: Axial strain poroelastograms of polyacrylamide-agar gels with (a) 1%C (b) 3%C (c) 4%C (d) 5%C. A 3x3 median filter was applied to the images for the purpose of illustration.
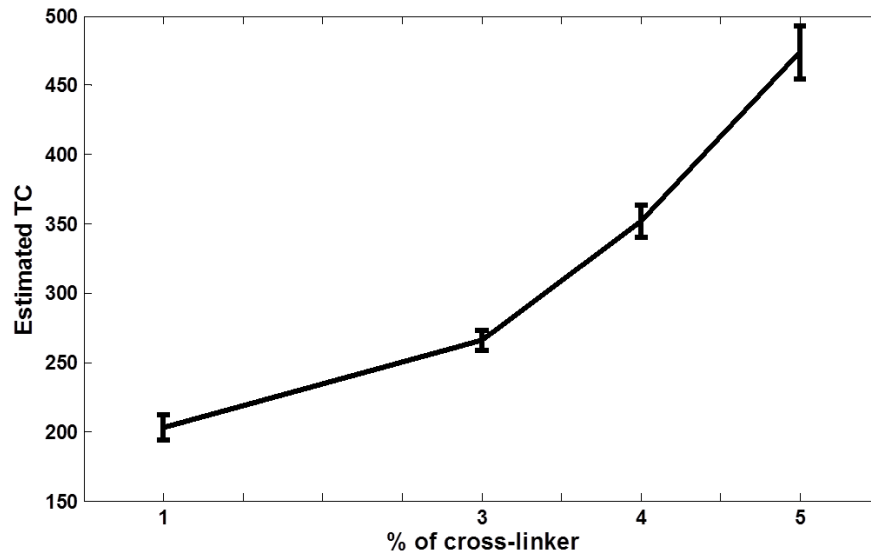
Figure 2.3: Estimated mean axial strain time constant (TC) measurements obtained from the homogeneous phantoms using axial strain data.

Figure 2.4 shows the axial strain poroelastograms obtained from the inclusion phantoms. The poroelastograms suggest different rate of changes for inclusion and background as the percentage of crosslinker is varied. As for the homogenous case, the strain increase in the background is much faster than in the inclusion for the first two cases where the background is more permeable than the inclusion. However for the third case (c) in which the background is less permeable (5%C) than the inclusion (1%C), there is no change between the two. In these cases, the inclusion is barely visible in the axial-strain images.
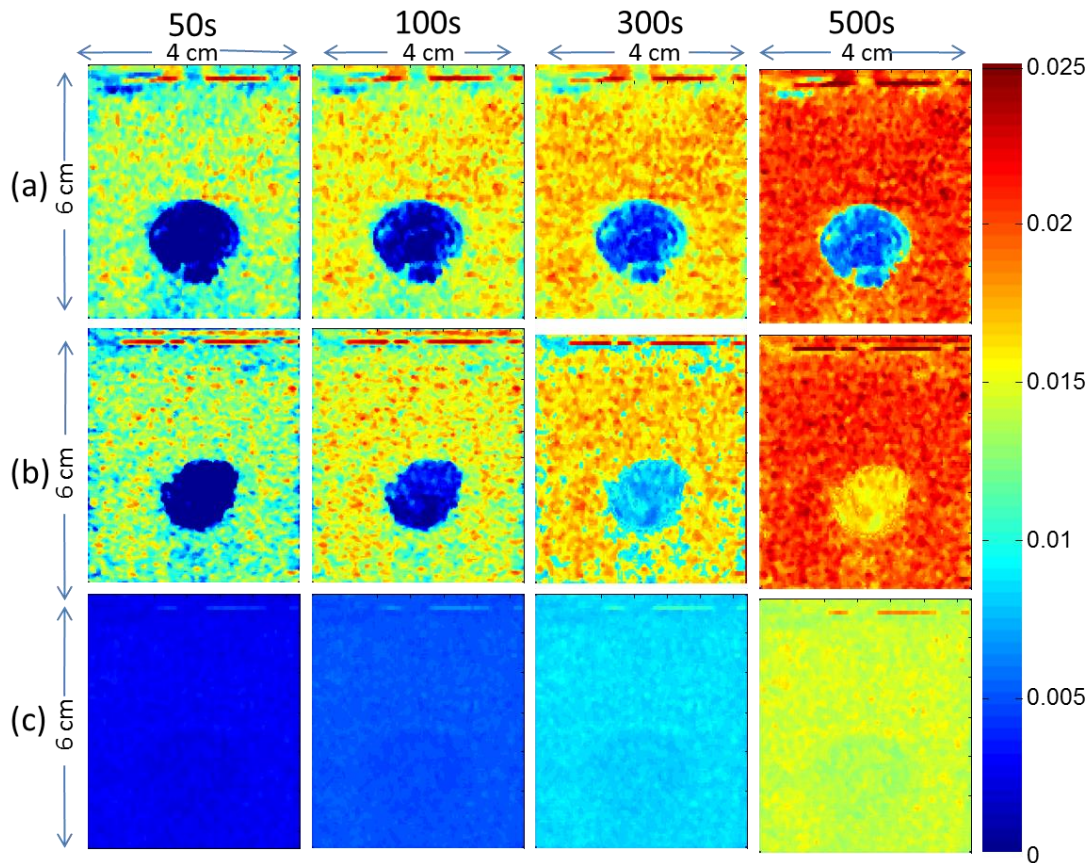
Figure 2.4: Axial strain poroelastograms obtained from three different polyacrylamide-agar phantoms with inclusion corresponding to the cases a, b and c given in Table 2.

These visual observations are confirmed by the estimated axial strain time constants reported in Table 4. These findings experimentally confirm some of our earlier simulation results (Chaudhry, et al. 2013). The measured SNRe was in the range of 9dB - 23dB in the uniform polyacrylamide gels, and the measured CNRe was in the range of 6dB - 20dB in the polyacrylamide gels with inclusion. These values are within the typical range of image quality elastographic measurements  (Srinivasan, et al. 2003).

| Inclusion Phantoms | Mean Axial Strain TC [s]<br><br>Background Region | Mean Axial Strain TC [s]<br><br>Inclusion Region |
|---|---|---|
| Case a | $210 \pm 10$ | $680 \pm 26$ |
| Case b | $212 \pm 7$ | $376 \pm 11$ |
| Case c | $471 \pm 21$ | $484 \pm 24$ |

Table 4: Estimated time constant (TC) values for inclusion phantoms with %C given by table 2.

Figure 2.5 shows a set of axial strain poroelastograms obtained from a 3% C

polyacrylamide gel (top row) and a standard agar gelatin phantom (bottom row) under

the same testing conditions.  No statistically significant temporal changes are observable

in the poroelastogram of the gelatin phantom, which explains the reason why this type of

phantoms is not suitable for temporal elastography studies. Figure 2.6 shows the post-

compression axial strain (mean) vs time in the two phantoms, confirming the results

shown in figure 2.5.
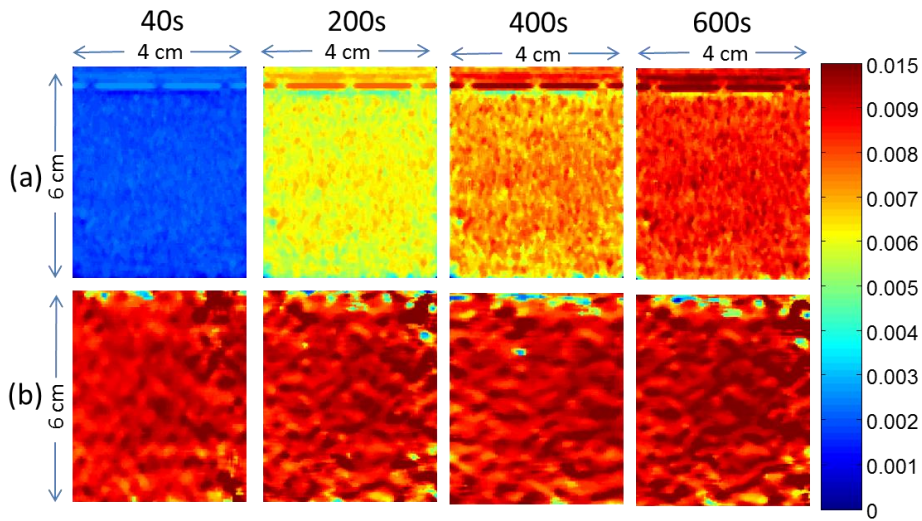
Figure 2.5: Axial strain poroelastograms of (a) polyacrylamide gel phantom made with 3% C and (b) gelatin phantom prepared with 5% gelatin and 3% agar.
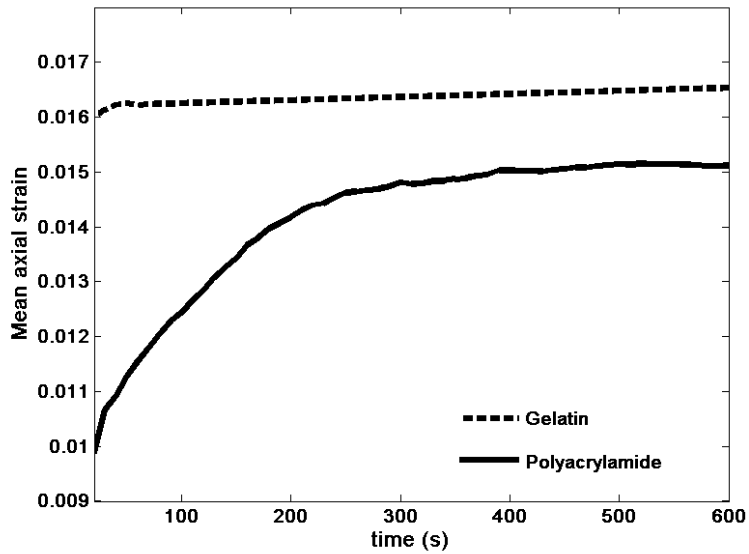


Figure 2.6: Mean axial strain vs time comparison of polyacrylamide gel and gelatin phantom.

## Discussion

In this paper, we report a new method to produce phantoms for poroelastography and, in general, temporal elastography imaging techniques in a reliable and controllable manner and with simple and inexpensive tools. Up to now, only very simplistic phantoms made out of gelatin or tofu has been used for these applications. We believe that the availability of the phantoms described in this paper may open the way to new and advanced controlled experimental studies involving these new elastography techniques and, in general, help moving the temporal elastography imaging field toward more clinically relevant yet controlled applications.

The newly proposed phantoms are made out of polyacrylamide gel, which has been used extensively in several applications but has not been investigated for temporal elastography studies yet. Being polymerized the gels created by this process have the advantage of being more stable than previously used phantoms in elastography such as gelatin and tofu(Bu-Lin, et al. 2008, Caulfield, et al. 2003, Kawabata, et al. 2004). The materials used are easy to retrieve and can be simply manipulated to create phantoms of complex geometries and fluid flow patterns with high reproducibility (Blattler, et al. 1972, Zakharov, et al. 1996). SEM imaging has been used to evaluate the pore size of the generated phantoms and its variation with the percentage of crosslinker. The SEM images show a significant decrease in pore sizes as the percentage of crosslinker is increased between 1% and 5%. These values were chosen based on previous studies, which noted that the smallest pore sizes were observed for a 5% concentration of cross-

linker and that the pore sizes and fluid mobility increased as this concentration was decreased (Holmes and Stellwagen 1991). Pore sizes also decrease with an increase of the acrylamide concentration i.e. monomer (T) (Blattler, et al. 1972, Holmes and Stellwagen 1991, Tombs 1965). For this study, we chose the concentration of T to be 5% so that the stiffness of the phantoms would be in the range of human tissues. However, a wide range of stiffness values can be obtained by varying the percentage of T between 1-20% (Baselga, et al. 1987, Galli, et al. 2009). In addition to similar mechanical properties, the addition of agar to the polyacrylamide mix allows to obtain phantoms with echogenicity properties similar to those used for standard ultrasound elastography experiments (Kallel et al., 1996).

The axial strain poroelastograms obtained from the polyacrylamide gels show that the temporal mechanical behavior of the phantoms due to fluid flow. In general, their temporal elastographic behavior changes with a change in pore size since this alters the fluid flow properties and permeability (White 1960). Figure 2.3 documents the axial strain time constants of the homogenous phantoms. Each individual concentration of crosslinker produced a statistically different (p<0.05) axial strain time constant. The axial strain time constant increases as the %C increases showing reduced fluid mobility. This change, however, is not linear with respect to the pore size as also confirmed by previous literature (Holmes and Stellwagen 1991). This non-linear dependence was also already observed by our group using simulation models (Chaudhry 2010, Chaudhry, et al. 2013). In the case of the non-homogenous phantoms, the axial strains in the inclusion and in the background change at statistically different rates due to difference in

25

permeability (p<0.05). In the cases where the background is more permeable than the inclusion, the axial strain time constants change significantly with changes in the percentage of the cross-linker. However, in the case where the background has smaller pore sizes than the inclusion, there is no statistical difference (p<0.05) between the axial strain time constants. This is due to a fundamental limitation of poroelastography techniques, defined as the contrast transfer efficiency for poroelastography (Chaudhry, et al. 2013, Kallel, et al. 1996, Ponnekanti, et al. 1995). The slower fluid flow in the background dictates the fluid flow rate in the inclusion. Hence, even though there is an underlying mechanical contrast in permeability, this cannot be measured using axial strain poroelastography. It can also be noted that the axial strain time constant of the inclusion in the non-homogenous phantom is significantly higher than the axial strain time constant measured in the homogenous phantoms having same %C. This is due to the different boundary conditions (the homogenous phantom has free boundaries on the sides while the inclusion is surrounded by the background) and is consistent with previous observations (Chaudhry 2010, Chaudhry, et al. 2013). Figures 2.5 and 2.6 show the comparison between the poroelastographic behavior overserved for a polyacrylamide gel phantom and the poroelastic behavior for a standard agar gelatin phantom. Although agar gelatin phantoms contain a significant amount of water, this water is bounded and cannot freely exude or move during compression. Since no change of volume occurs under compression, gelatin phantoms are typically not considered as poroelastic. The axial strain data reported in figures 2.5 and 2.6 confirm that very little axial strain temporal changes occur in agar gelatin phantoms under compression. A

direct comparison with the temporal data reported for the polyacrylamide gels in the same figures (and in the rest of this article) demonstrates the need and advantage of using these novel poroelastography phantoms for temporal elastography studies.

## Conclusion

In this paper, we present a novel methodology to generate homogeneous and inhomogeneous phantoms for ultrasound poroelastography. We show that it is possible to create tissue-mimicking phantoms with controlled pore size and fluid mobility using polyacrylamide gels while maintaining similar mechanical and ultrasonic properties as those of phantoms used for standard elastography experiments. In addition to poroelastography, this new class of phantoms may be useful to test different temporal elastography techniques and applications.

# 3. FEASIBILITY OF ESTIMATING POISSON'S RATIO IN NON-HOMOGENOUS POROUS MEDIA USING TWO ULTRASOUND TRANSDUCERS

## Introduction

Most biological tissues such as cartilage, brain, liver, kidney, breast and prostate have high fluid content and are poroelastic in nature tissues (Abbott 2004, Fatt 1968, Jain 1994, Jurvelin, et al. 1997, Mow, et al. 1984, Van Houten, et al. 2003). A poroelastic material is defined as a bi-phasic material in which at least one of the phases is solid (Wang 2000). For tissues the two phases consist of the solid interstitial matrix while the interstitial fluid makes up the fluid phase(Armstrong, et al. 1984). Ultrasound elastography imaging is a well-established technique which has been shown to reliably map tissue stiffness (Ophir, et al. 1999, Ophir, et al. 1991). Poroelastography is a branch of ultrasound elastography which aims at assessing the poroelastic properties of tissues (Berry, et al. 2006, Konofagou, et al. 2001, Raffaella, et al. 2007). The hypothesis of poroelastography is that underlying pathology such as cancer alters the underlying fluid flow properties which alter the poroelastic response of the tissue under compression (Righetti, et al. 2004). Most cancers such as that of the breast, neck, prostate, liver are known to possess altered fluid transport due to collapse of the interstitial matrix, cellular deposition, leaky microvasculature and weak lymphatic drainage (Boucher, et al. 1991, Boucher, et al. 1997, Gutmann, et al. 1992, Hassid, et al. 2006, Heldin, et al. 2004, Jain 1987, Nathanson and Nelson 1994, Roh, et al. 1991). These mechanisms lead to high

interstitial fluid pressure and lower interstitial permeability of the tumor tissue. (Heldin, et al. 2004)

Poroelastography techniques aim at assessing the poroelastic response of a tissue by observing the spatial and temporal behavior of axial strains and 'effective' Poisson's ratio (EPR) on compression (Righetti, et al. 2005). The EPR image is obtained as the ratio between the lateral strain elastogram and the corresponding axial strain elastogram (Righetti, et al. 2004). A poroelastic material by definition is compressible, i.e. it allows fluid movement and change in volume upon compression. These mechanisms cause a change in the spatial and temporal behavior of EPR, which is an important parameter because it is related to true changes in volume of the material due to fluid flow rather than viscoelastic changes. However, the image quality of EPR elastogram is limited by of the poor quality of standard lateral strain elastography (Kallel, et al. 1997, Konofagou and Ophir 1998, Lubinski, et al. 1996). To improve the quality of lateral strain elastography and EPR, some studies have implemented advanced filtering techniques combined with spatial, temporal and multi-experiment averaging (Raffaella, et al. 2007, Righetti, et al. 2005). Experimentally averaging is not just difficult it is highly time consuming. Also experimental conditions including motion of subject, fluid content etc. may change between experiments. These limitations make the technique unfavorable for clinical applications. Recently a technique that employs two transducers was proposed to improve 2D axial displacement estimation by improving lateral tracking (Abeysekera, et al. 2012). The study showed the feasibility of improving lateral tracking using two transducers instead of one for quasi-static elastography of linearly elastic materials.

However it did not address its implications to the field of poroelasticty imaging. In this study we explore the feasibility of using a two transducer technique to image the EPR in a single experiment with high image quality and reliability.

## Materials and methods

### Finite element simulations

To test the feasibility of the study  finite element analysis (FEA) similar to that used in (Chaudhry, et al. 2013) was performed.  Specifically a tumor model with different fluid flow properties between the inclusion and background was simulated. We used a 40x40 mm 2D rectangular domain with a circular inclusion of 15mm diameter embedded in the center.  Baseline material properties were chosen in the range of human tissues on the basis of that reported previously in literature (Chaudhry, et al. 2013, Nair, et al. 2011, Netti, et al. 2000, Righetti, et al. 2005). Young's modulus and Poisson's ratio were fixed at 1.74 kPa and 0.25 respectively. To vary the fluid flow, permeability was varied between the background and the inclusion as listed in table 1. Creep compression was simulated between two impervious plates for 600 seconds. To emulate the experimental conditions axial and lateral displacements were generated at every 0.5 second time points. There parameters were chosen based on previous studies conducted in our lab (Nair, et al. 2014, Nair, et al. 2011). Pre and post compression ultrasound RF data was simulated using a convolution model (Chaudhry 2010, Kallel and Bertrand 1996, Kallel, et al. 2001). The simulated ultrasound transducer had 128 elements, frequency bandwidth between 5-14 MHz, a 6.6 MHz center frequency and 50% fractional

bandwidth at -6 dB.  The transducer's beam-width was assumed to be dependent on the

wavelength and to be approximately 1 mm at 6.6 MHz (Kallel, et al. 2001).  The

sampling frequency was set at 40 MHz and Gaussian white noise was added to set the

SNRs at 40db. Axial strains were computed for both transducers at each time sample

using cross-correlation based elastography algorithm (Ophir, et al. 1996, Raffaella, et al.

2007). The length of the correlation window, both for the pre- and post-compression

signals, was fixed at 1.5 mm with an 80% overlap between adjacent windows.

| Contrast | Permeability Inclusion k (m⁴/N.s) | Permeability background k (m⁴/N.s) |
|---|---|---|
| 10 dB | $1.95 \times 10^{-9}$ | $1.95 \times 10^{-8}$ |
| 20 dB | $1.95 \times 10^{-10}$ | $1.95 \times 10^{-8}$ |
| 25 dB | $9.75 \times 10^{-10}$ | $1.95 \times 10^{-8}$ |
| 30 dB | $1.95 \times 10^{-11}$ | $1.95 \times 10^{-8}$ |

Table 5: Permeability values used for inclusion back background material for given contrast.


**Experimental setup**

Three non-homogenous phantoms were created using tofu (Banyan foods, Houston, TX)

with a gelatin inclusion embedded in it. These phantom materials were used to be

consistent with  previous poroelastography studies (Righetti, et al. 2004). The size of the tofu was 6cm x 6cm x 6cm with a cylindrical gelatin inclusion of 15 mm diameter.  The gelatin inclusion was created by mixing 5% porcine gelatin (Sigma-Aldrich, USA) with 3% agar (Sigma-Aldrich, USA) as in (Kallel, et al. 2001). Figure 3.1 shows the experimental setup used in the study. The phantom was compressed between the two plates using creep compression for 600 seconds (Nair, et al. 2011). Elastography experiments were performed using two 128 elements Ultrasonix RP (Richmond, Canada) linear array scanner with 1mm beam width, 50% fractional bandwidth and 6.6 MHz center frequency. Firing of both the transducers at the same time led to acoustic interference of ultrasound pressure waves scanning the same plane. To avoid this noise ultrasound RF data was acquired alternatively by the axial and lateral transducers with a time difference of 0.5 seconds between the acquisitions. Axial strains were computed for both transducers at each time sample using cross-correlation based elastography algorithm (Raffaella, et al. 2007). The length of the correlation window, both for the pre- and post-compression signals, was fixed at 1.5 mm with an 80% overlap between adjacent windows.  Experiments were carried out under water to maintain good ultrasonic connectivity between the phantom and the lateral transducer. Strain images from the two transducers were computed in the same way as for the simulation data. To reduce de-correlation noise axial strains at each time point were computed as a cumulative sum up to that point (Righetti, et al. 2005).
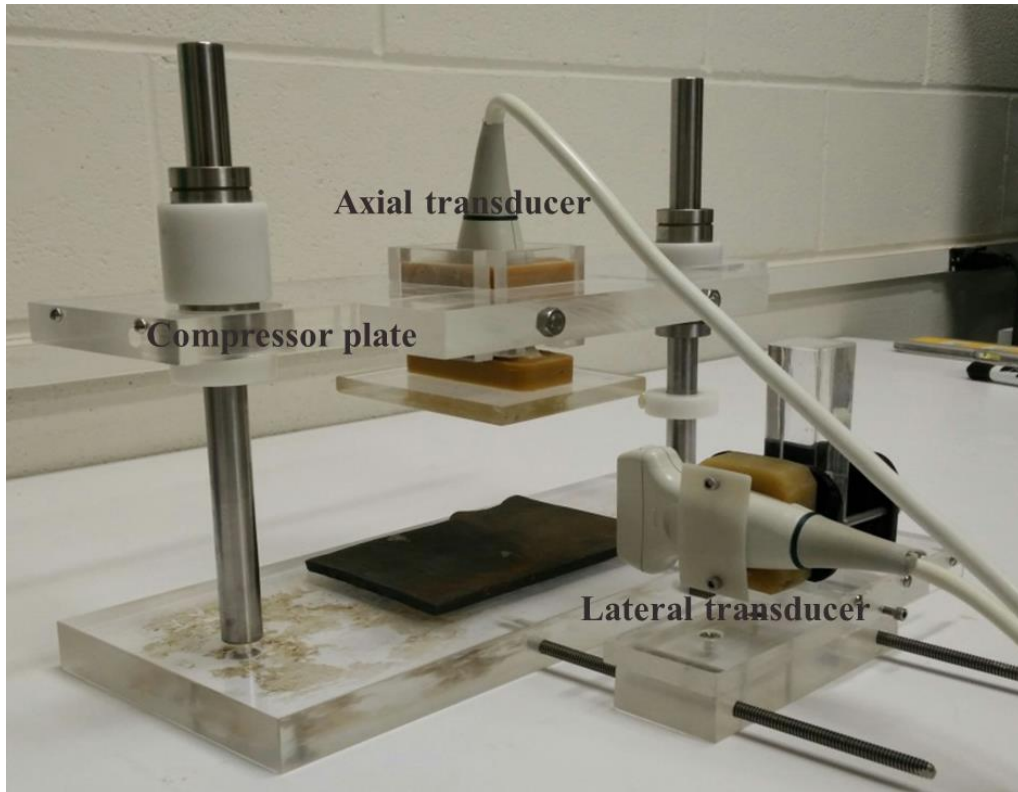
Figure 3.1: Experimental setup used for the two-transducer technique.

**Estimation of EPR poroelastogram**

For reliable estimation of EPR the two transducers should scan the same image plan and

should be orthogonal to each other.  To address these constraints the transducers were

manually calibrated using an image based calibration technique. A rectangular

calibration phantom (40mm x 20mm x 1mm) as shown in figure 3.2 was 3D printed

from ABS plastic.  Two B mode images from each transducer were obtained and the

specular reflection from the two orthogonal edges was segmented out and their angle

with respect to each other was calculated.  By mechanically adjusting the two

transducers we were able to reduce the error to less than 0.1°.Image registration was

performed using a feature based segmentation technique. The inclusion was segmented

in each temporal frame using thresholding and morphological reconstruction.
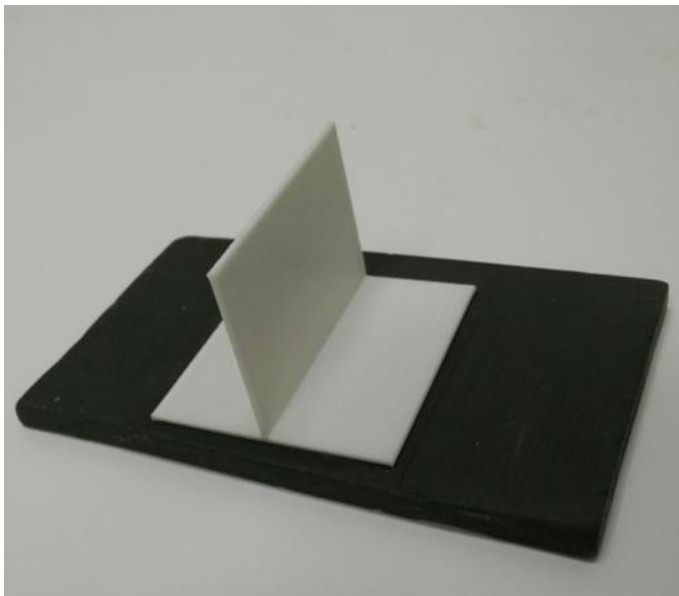


Figure 3.2: The calibration phantom used to calibrate the axial and lateral transducers.

The centroid of the inclusion was then found and used as an input to affine

transformation which rotated and translated the lateral strain image to the co-ordinates of

the axial (Lamdan, et al. 1988). The EPR image was then estimated by dividing the

registered lateral strain image by the axial.  The EPR poroelastogram was displayed as

time-sequenced images of EPR (Righetti, et al. 2005).

**Image quality analysis**

To analyze the simulated poroelastograms we used two parameters than have been previously used in elastography studies- the elastographic contrast to noise ratio (CNRe) and the mean absolute error (MAE). The EPR CNR$_e$ has been defined as (Raffaella, et al. 2007).

$$PCNR_e = \frac{2\ (v_t - v_b)^2}{\sigma_t^2 + \sigma_b^2} \quad \text{.............................................................................................. (2)}$$

Where $v_t$ is the estimated EPR of the inclusion and $v_b$ is the estimated EPR of the background and σt and $\sigma_b$ are the corresponding standard deviations.

The MAE provides an assessment of the accuracy of estimation as compared to the expected or true value. The lower the MAE the higher the accuracy. MAE is mathematically defined as:

$$MAE\ (\%)\ = \frac{1}{xy} \Sigma \frac{abs(EPRe(xi,yj) - FEA(xi,yj))}{FEM(xi,yj)}\ x\ 100 \quad \text{................................................. (3)}$$

Where EPRe is the estimated EPR and FEA and is true or actual value of EPR. We used CNRe and MAE to compare the performance of the two-transducer (TT) elastography technique with that of a single transducer, multi-experiment averaging (MEA), and that obtained from the true value in FEA.

**Results**

To evaluate the performance of the two transducer technique we compared the estimated

two-transducer EPR poroelastograms with that generated from FEA (true value), single

transducer implementation and single transducer with 30 independent experiment

averaging. Figure 3.3 shows the corresponding poroelastograms for a 25 dB permeability

contrast between the inclusion and background. It can be seen that the two transducer

technique has the closest resemblance to the FEA results, followed by the multi

experiment averaging technique. To analyze these observations we compared the

temporal EPR CNRe and MAE of these cases as shown in figure 3.4 and figure 3.5

respectively. The estimated CNRe was lowest for the single transducer implementation

and highest for the ones estimated from FEA.
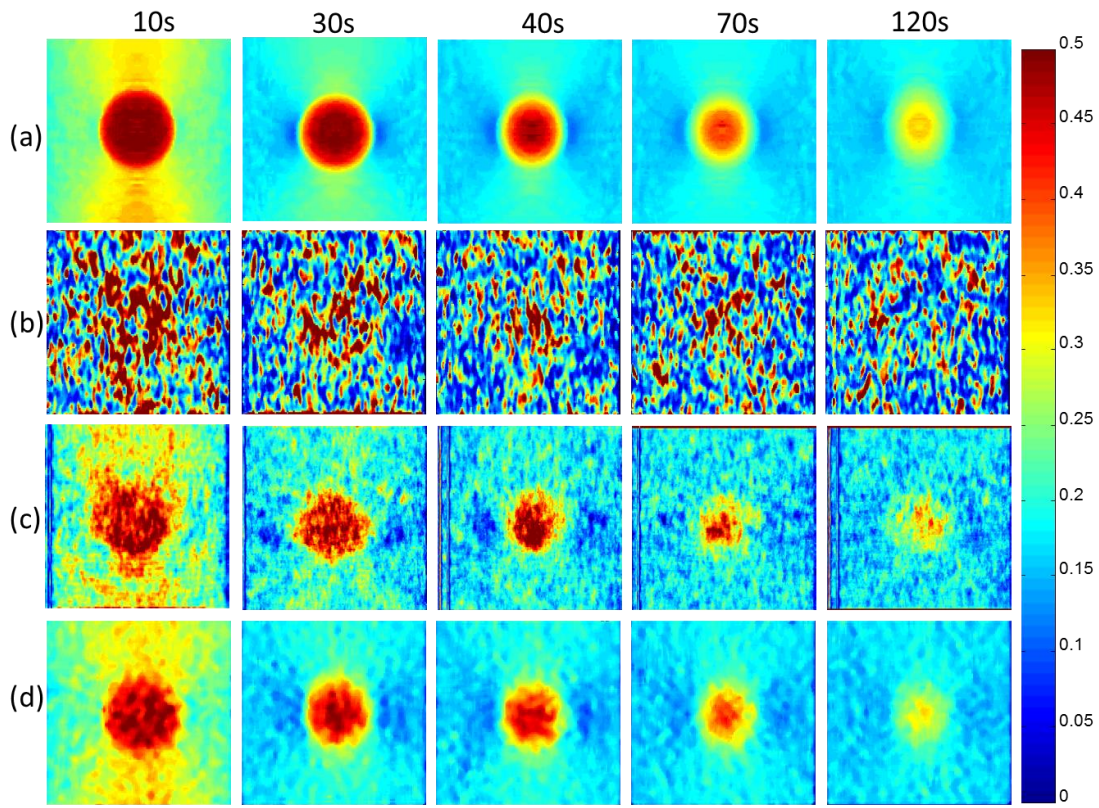
Figure 3.3: EPR poroelastograms for a 25 dB permeability contrast generated by (a) FEA (b) Single transducer (c) Single transducer with 30 experiment averaging and (d) two-transducer method. For the purpose of illustration, a 5 x 5 pixels median filter was applied to each image.

The two transducer technique had a higher CNRe than the previously used multi-experiment averaging method. Similar results were observed for the MAE plots. The MAE of the single transducer method was the highest followed by the multi-averaging version. The MAE of dual transducer FEA shows the error included by the 0.5 s sampling gap between the lateral and axial acquisitions.
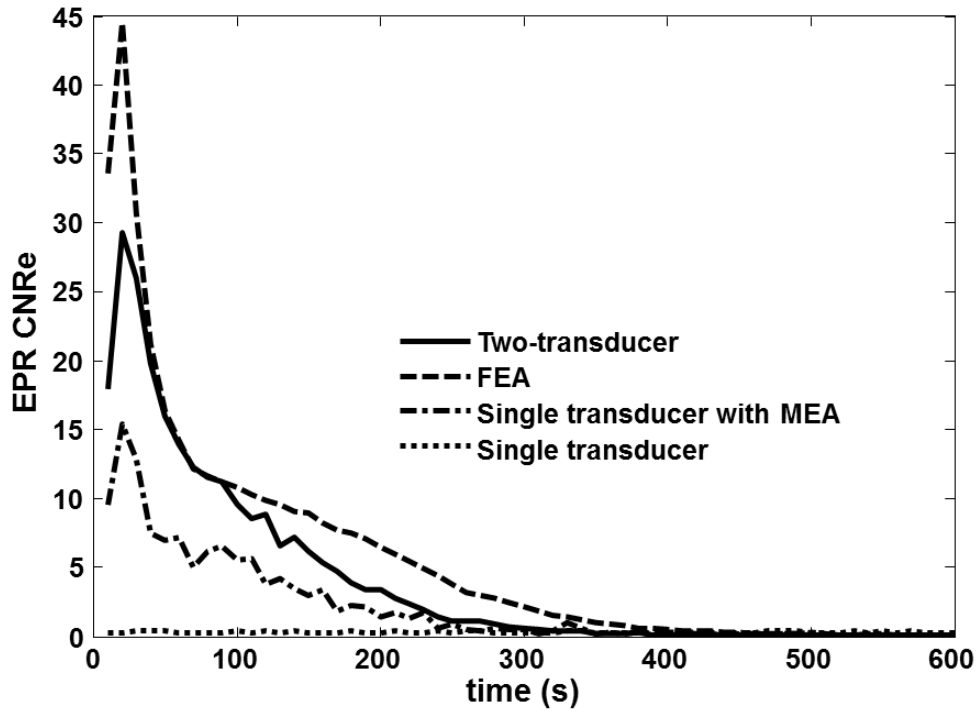
Figure 3.4: EPR CNRe comparison between the two-transducer, FEM, Single transducer 3with multi-experiment averaging (MEA) and single transducer with no averaging.

Figure 3.6 shows the EPR poroelastograms with different permeability contrast between the inclusion and background. A contrast in the underlying permeability creates a contrast in the corresponding poroelastograms. Figure 3.7 shows the EPRCNRe for the two transducer poroelastograms with different contrast between the inclusion and the background. It can be observed that both the peak and temporal behavior of EPRCNRe varies with underlying permeability contrast.
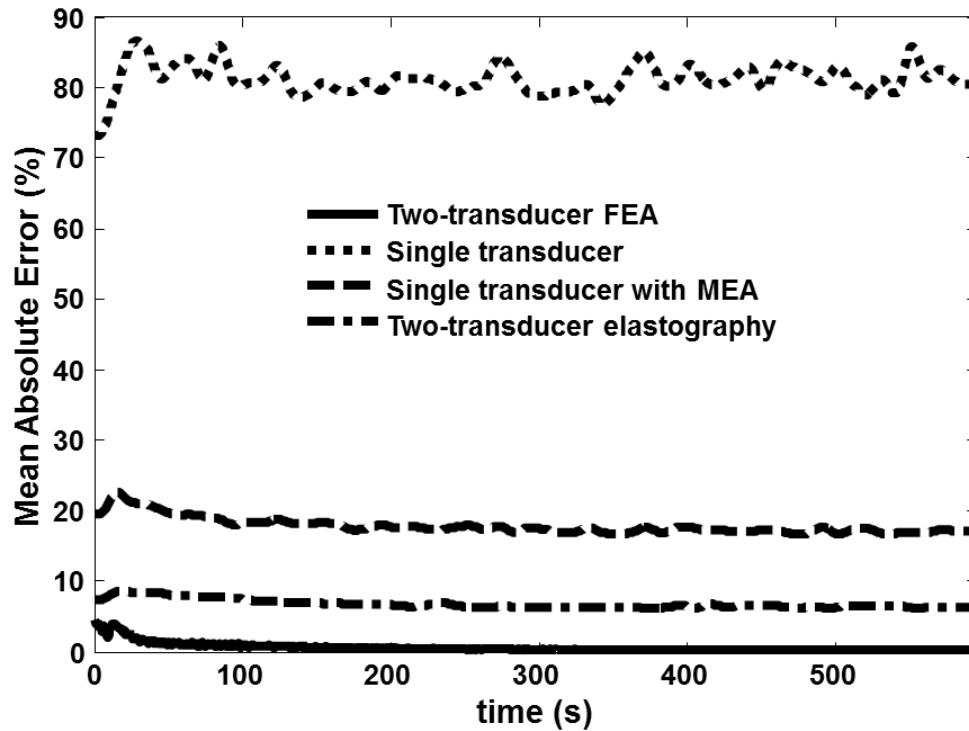
Figure 3.5: Mean absolute error (MAE) comparison between the two-transducer FEA, Single transducer multi- experiment averaging (MEA), single transducer with no averaging and two-transducer elastography technique

Figure 3.8 depicts the EPR poroelastogram generated from the tofu-gelatin phantom. It can be observed that there is minimal temporal change in the EPR of the gelatin inclusion while the EPR of the tofu material decreases from 0.5 to its equilibrium value of around 0.2. In figure 3.9 the mean and standard deviations of the estimated EPR are presented with time.
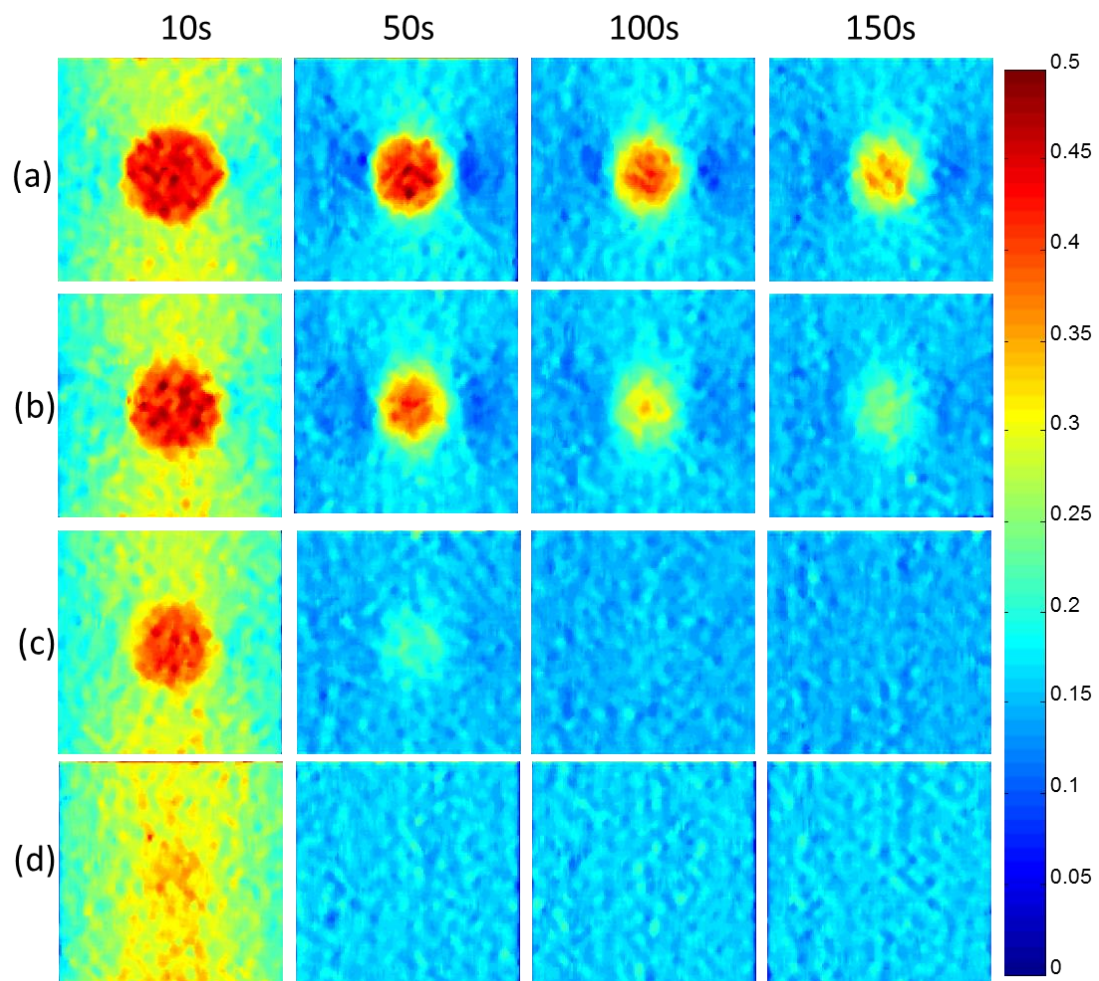
Figure 3.6: EPR poroelastograms obtained using the two-transducer method for (a) 30 dB (b) 25 dB (c) 20 dB and (d) 10 dB contrast between the inclusion and background. For the purpose of illustration, a 5 x 5 pixels median filter was applied to each image.
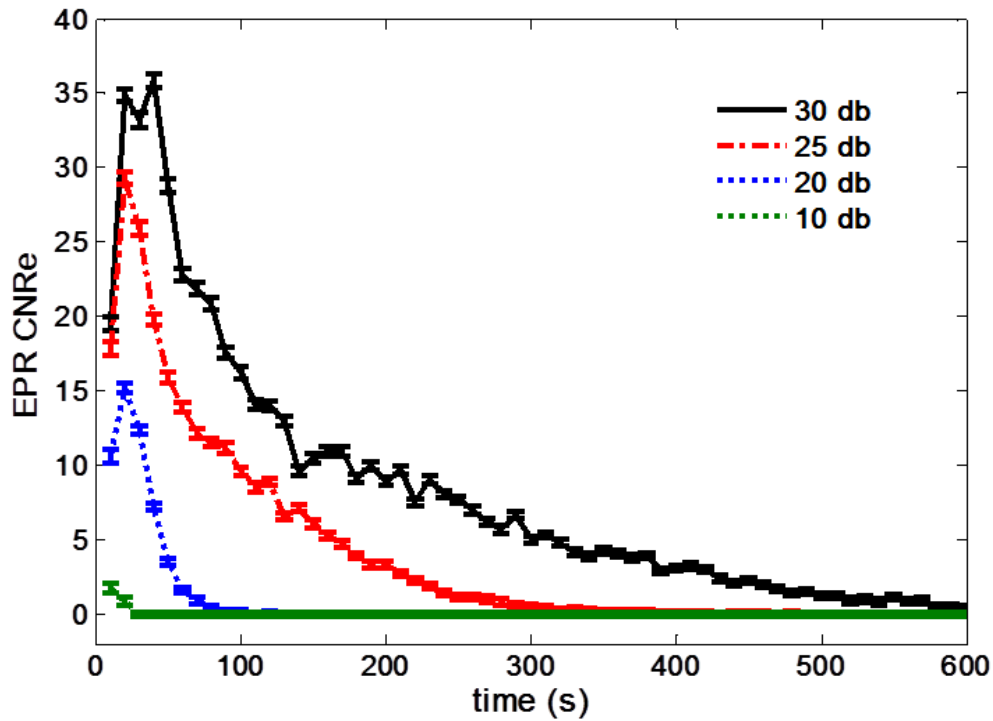
Figure 3.7: EPR CNRe plot for the two-transducer elastography technique for different contrast between the background and inclusion.

**Discussion**

Most cancers have altered pore structure which alters their ability to change volume upon compression. Poroelastography techniques aim to assess these altered fluid transport mechanisms by observing the temporal behavior of EPR upon compression. The EPR is calculated by dividing the lateral strain elastogram by the corresponding axial strain. However reliable estimation of EPR is currently very difficult due to the known limitations in estimation of lateral strains (Lubinski, et al. 1996). These limitations stem from the ultrasound transducer itself which has restriction on the

number and size of elements which limit the number of samples/mm in the lateral direction as compared to axial. Previous techniques to improve lateral strain elastography include increasing the number of samples by using weighted interpolation and/or reducing the noise by temporal averaging and averaging independent experiments. All of these techniques have shown promising improvement however have inherent limitations. They are also based on interpolation/averaging of the limited lateral data and do not add any new information. In this study we propose the use of a second transducer to image the lateral strain caused due to the compression in the axial direction. By doing so we can estimate the lateral strains with high image quality and reliability. The division of two axial strains can result in reliable estimation of EPR in a single acquisition.
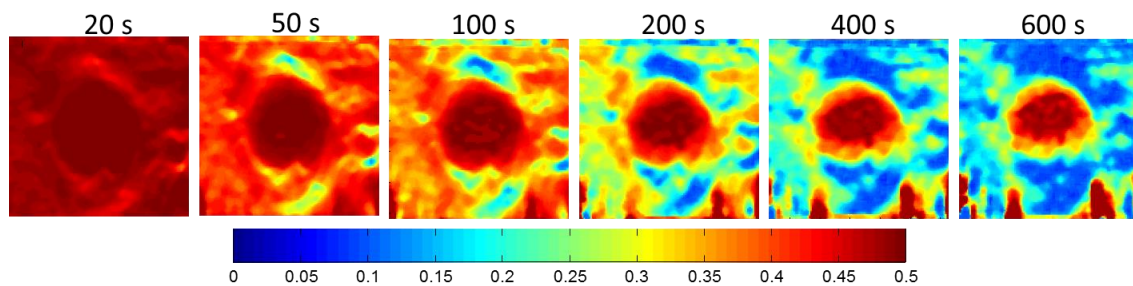


Figure 3.8: EPR poroelastogram obtained from the tofu-gelatin inclusion phantom using the two-transducer technique. For the purpose of illustration, a 5 x 5 pixels median filter was applied to each image.

In figures 3.3-3.5 we compare the performance of the two-transducer technique with the multi-experiment averaging technique used previously in poroelastography studies(Raffaella, et al. 2007, Righetti, et al. 2005). The poroelastograms from the two-transducer technique show that there is a clear visual improvement in image quality between the two. The images from the two-transducer poroelastograms also closely resemble to that simulated by FEA. These visual observations were quantitatively analyzed and reported in the EPR CNRe and MAE plots. The peak EPR CNRe of the TT technique was 1.9 times higher and the peak MAE was 1.94 times lower than the multi-experiment averaging technique. The poroelastograms and the image quality analysis clearly indicate that the two transducer technique has superior performance over the currently available estimation methods.
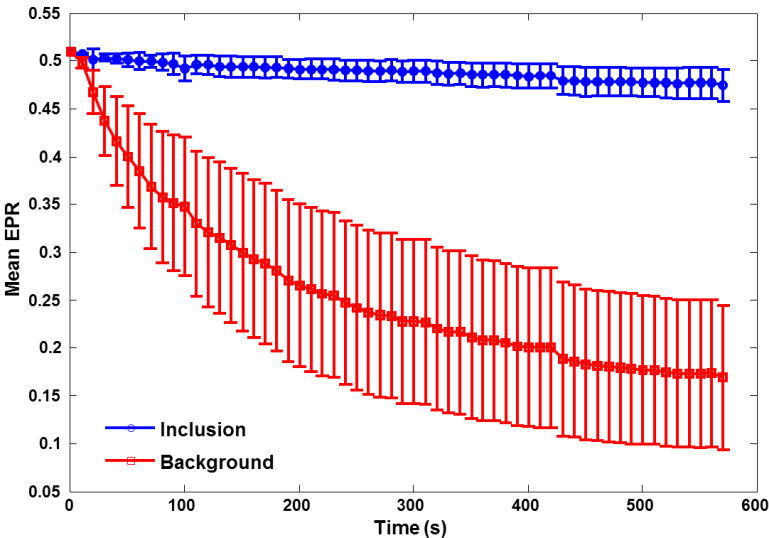


Figure 3.9: Mean estimated EPR with time.

Figure 3.6 shows the TT-EPR poroelastograms with different contrast of permeability between the inclusion and background. It can be observed that a contrast in the underlying permeability creates a contrast in the corresponding poroelastograms which changes with simulated contrast. For lower values of permeability of the inclusion (i.e. higher contrast), the inclusion EPR takes longer to reach its equilibrium value. These results confirm the ones observed in (Chaudhry 2010, Chaudhry, et al. 2013, Righetti, et al. 2004). Figure 3.7 documents the EPR CNRe obtained from the poroelastograms reported in figure 3.6. It can be seen that the peak CNRe value increases with contrast. Also with increasing contrast the inclusion takes longer to reach its equilibrium value which is also reflected in the corresponding EPR CNRe graphs.

Figure 3.8 depicts the EPR poroelastogram obtained by experimental implementation of the two-transducer technique. As expected from previous studies the experimental images are noisier than simulations (Righetti, et al. 2005, Righetti, et al. 2004). Both tofu and the gelatin in the inclusion behave as nearly incompressible materials and have an EPR around 0.5 initially (Armstrong, et al. 1984). However with time after compression, tofu drains out water, loses volume and its EPR reduces towards its equilibrium value. The EPR of the gelatin inclusion can be seen to be nearly constant at 0.5. This is because even though the gelatin consisted of over 80% water, the fluid phase was not able to move with respect to the solid matrix making it incompressible. These results confirm the ones observed in (Righetti, et al. 2004). Figure 3.9 shows the temporal curves of the mean estimated EPR in both the inclusion and the background. It

can be observed that the EPR in the background decays exponentially with time whereas there is minimal linear change in the EPR of the inclusion.

The current experimental setup has some limitations and it is not ready to be used for in-vivo studies. Due to the positioning of the ultrasound transducers and compressor plates there is a limit on the geometry and size of the sample under investigation. The current Ultrasonix system we used had the capability of using two transducers as an input, however switching between them is done by a mechanical relay switch. For this reason we had to use two separate systems each for axial and lateral data acquisition. In future if the switching between the transducers could be controlled by an electronic switch, a single system can be successfully used. Also, in this study we computed the EPR by alternate acquisition of the axial and lateral transducers using a sampling. We used a sampling time of 0.5 seconds which minimized the error to less than 3.5%. However for shorter and faster changing EPR values a lower sampling time will be required to minimize errors caused between lateral and axial acquisitions.

## Conclusion

In this paper we show the proof-of-principle of estimating the temporal behavior of EPR using two ultrasound transducers. Simulation results show that using this technique it is possible to generate EPR poroelastograms with high contrast-to-noise ratio and low mean absolute error. We also demonstrated the experimental feasibility of the technique using non-homogenous phantom. The experimental implementation in its current form has some limitations which warrant further investigation.

4. EFFECT OF INTERSTITIAL FLUID FLOW ON THE TEMPORAL BEHAVIOR OF INTERSTITIAL FLUID PRESSURE ON UNI-AXIAL COMPRESSION – IMPLICATIONS ON ULTRASOUND POROELASTOGRAPHY

**Introduction**

Interstitial fluid pressure (IFP) has been shown to be of high importance in the case of soft tissue cancers (Boucher, et al. 1990, Heldin, et al. 2004). Most cancers including that of the breast, lung, neck and head, cervix, skin, brain, and con-rectal have been shown to possess elevated IFP (Milosevic, et al. 2001, Milosevic, et al. 2008, Nathanson and Nelson 1994, Roh, et al. 1991) (Hassid, et al. 2006, Kristjansen, et al. 1993) (Boucher, et al. 1991) (Boucher, et al. 1997, Gutmann, et al. 1992). High IFP in malignant tumors may be due to many factors including collapse of interstitial matrix, weak lymphatic drainage and changes in microvasculature responsible for the trans-capillary transport (Heldin, et al. 2004, Milosevic, et al. 2008) each of which cause a decrease in interstitial permeability and higher IFP (Jain 1987). This increased pressure has not just been used to detect and classify tumors but has also been shown to be a major factor impeding target drug delivery techniques. Due to this reason many therapeutic techniques are being developed to lower IFP before delivering the drug (Frenkel, et al. 2006, Griffon-Etienne, et al. 1999, Kristjansen, et al. 1993, Watson, et al. 2012). Most of the techniques that measure IFP such as the wick-catheter (Scholander, et al. 1968), wick-in-needle (Fadnes, et al. 1977), glass micropipette , semiconductor tipped (Ozerdem and Hargens 2005) are invasive. Recently interest in non-invasive

measurement of IFP has resulted in a few studies using MRI and optical methods (Hassid, et al. 2006, Hompland, et al. 2012, Ozsun, et al. 2014, Walker-Samuel, et al. 2012). No ultrasound method currently exists for non-invasive assessment of IFP. Ultrasound elastography is a well-established imaging modality used to map the local strains of a soft tissue under quasi-static compression (Ophir, et al. 1999, Ophir, et al. 1991). Many elastography studies have aimed to analyze the detectability of these tumors based on their stiffness (Ginat, et al. 2009, Hiltawsky, et al. 2001). The results are often interpreted based on modelling the tumor as linearly elastic incompressible solid (Kallel and Bertrand 1996). Under these assumptions a contrast in the axial strain elastograms is interpreted as a contrast in underlying elastic modulus of the tissue (Doyley 2012). The effect of elevated IFP on US elastography technique is largely unknown. Knowledge of the effect of this parameter may aid in future interpretations of application of elastography technique to tumors, especially for cases with known elevated IFP.

Poroelastography is a branch of ultrasound elastography that aims at imaging the temporal response of tissues under compression(Righetti, et al. 2004). The hypothesis of poroelastography is that the altered fluid transport mechanisms caused due to change in permeability and fluid pressure in cancers alters their poroelastic response(Chaudhry, et al. 2013). This change is response can be assessed by estimating the temporal behavior of axial strains and 'effective' Poisson's ratio (EPR)(Righetti, et al. 2005, Righetti, et al. 2007). For a poroelastic material under uni-axial compression, the temporal response is governed by fluid translocation mechanisms which in turn depends on local pressure

47

gradients (Armstrong, et al. 1984). Upon compression the material changes volume due to exudation of fluid resulting is pressure relaxation, which also causes the EPR of the material reduces from about 0.5 (nearly incompressible) to its equilibrium value(Righetti, et al. 2005). However the relationship between poroelastography parameters and underlying fluid pressure (IFP) is not known. Investigation of relationship between the temporal behavior of EPR and IFP may encourage future research in the use of US poroelastography techniques for non-invasive assessment of underlying fluid pressure.

In this study we investigate the effect of elevated IFP caused due to altered interstitial fluid flow on the resulting axial strain and EPR images. We also evaluate the relationship between the spatio-temporal behavior of axial strain, EPR and IFP under uni-axial compression.

## Materials and methods

### Theoretical consideration of porous media

We assumed a porous media that is fully saturated with fluid. The solid and fluid phases are assumed to be homogeneous, isotropic, and chemically inert. The behavior of porous media is governed by two conservation laws: mass conservation for the fluid phase and conservation of linear momentum for the solid phase in a porous medium. The continuity equation (equation of mass conservation) for the fluid phase is given by (Chaudhry, et al. 2013, Systèmes 2012)

$$\left[\left(\frac{\partial \xi}{\partial t}\right) + \nabla q\right] = \Upsilon \quad \text{(4)}$$

48

where $\zeta$ is the variation of fluid content per unit volume of porous media, q is the flux

(discharge of fluid per unit area), and $\gamma$ is the rate of injected fluid volume per unit

volume of the porous media. In steady-state case, there are no transient effects in Eq. (1)

and thus the flux q is constant. In order to describe the fluid transport, we adopted

Darcy's law which states that, under uniform conditions, the volumetric flow rate of the

fluid through a unit area of porous solid is proportional to the negative fluid pressure

gradient:

$$q = -\frac{k}{\mu f} \nabla p \quad \text{................................................................................................ (5)}$$

where $k$ is the intrinsic permeability having dimension of length squared and $\mu_f$ is the

fluid viscosity. Secondly, the equation of conservation of linear momentum for the solid

phase in a porous medium is given by

$$\nabla \cdot \sigma + f = 0 \quad \text{................................................................................................ (6)}$$

where σ and f are the total stress tensor and body force per unit volume, respectively. In

this study, the body force is assumed to be negligible. The total stress tensor σ consists

of the fluid pressure, called pore pressure, $p$ and effective stress $\boldsymbol{\sigma}$ as

$$\sigma = \boldsymbol{\sigma} - pI \quad \text{................................................................................................ (7)}$$

where I is the identity tensor.

**Finite element analysis**

A 2D in-house finite element analysis (FEA) similar to that used before was

implemented in FORTRAN (Chaudhry 2010, Chaudhry, et al. 2013). The analysis

assumed a linear stress-strain behavior of the solid phase and a single fluid flowing

through the saturated media obeying Darcy's flow law. These two phases are coupled

using Biot's constant (alpha) and the specific storage coefficient, which depends on the

undrained and drained material properties.  Once the basic equations are set up, the finite

element development with the displacement and pressure as the primary variables is

carried out(Chaudhry 2010). Details of the analytical model and finite element

implementation have already been documented in a previous study by our group

(Chaudhry, et al. 2013)and will not be repeated here.

 Two kinds of models were simulated with different geometries which have been used

before in elastography studies- the homogenous and inclusion model (Chaudhry, et al.

2013, Kallel, et al. 2001, Konofagou, et al. 2001). The homogenous model consisted of

axisymmetric 40 x 40 mm rectangle of uniform poroelastic material. Similarly, the non-

homogenous or inclusion model consisted of a 40 x 40 mm rectangle with a circular

inclusion of 15mm diameter embedded in the center. For both models friction less

boundary conditions were prescribed at the bottom whereas the ones on the sides were

free boundaries. Poroelastic material properties were used based on previous

experimental work(Righetti, et al. 2005). For the homogenous case the interstitial

permeability (k) was varied between $1.95 \times 10^{-9}$ m$^4$/N.s to $1.95 \times 10^{-8}$ m$^4$/N.s. For the

inclusion case the permeability of the background material was fixed at $1.95 \times 10^{-8}$ and

that of the inclusion was varied between $1.95 \times 10^{-8}$ m$^4$/N.s and $1.95 \times 10^{-10}$ m$^4$/N.s giving

rise to a contrast between 5 dB and 20 dB between the inclusion and the background.

 To simulate the poroelastography experiments the two phantoms were compressed

between two impervious plates.  The temporal window of observation was chosen to be

600s and the time sample was chosen to be 0.5 seconds. These parameters were chosen based on previous experimental work done in the field of poroelastography (Nair, et al. 2014, Nair, et al. 2011). Axial and lateral displacements were calculated at each time point and corresponding strains were simply computed as the gradient of the displacements. The effective Poisson's ratio (EPR) image was computed by dividing the lateral strain by the axial. The temporal behavior of IFP, axial strain and EPR was quantified by estimating the mean time constant (TC) of the temporal curve using a least square error (LSE) curve-fitting method (Nair, et al. 2011). The standard deviation was specified by calculating the TC estimation error (Nair and Righetti 2015).

## Results

Figure 4.1 shows the temporal images of IFP, EPR and axial strain for the homogenous phantom with the underlying interstitial permeability k= $1.95 \times 10^{-9}$ m$^4$/N.s. The temporal behavior of IFP changes with time and the time it takes for the pressure to relax i.e. reach zero is visually comparable to the time it takes for the axial strain and EPR to reach their equilibrium values.
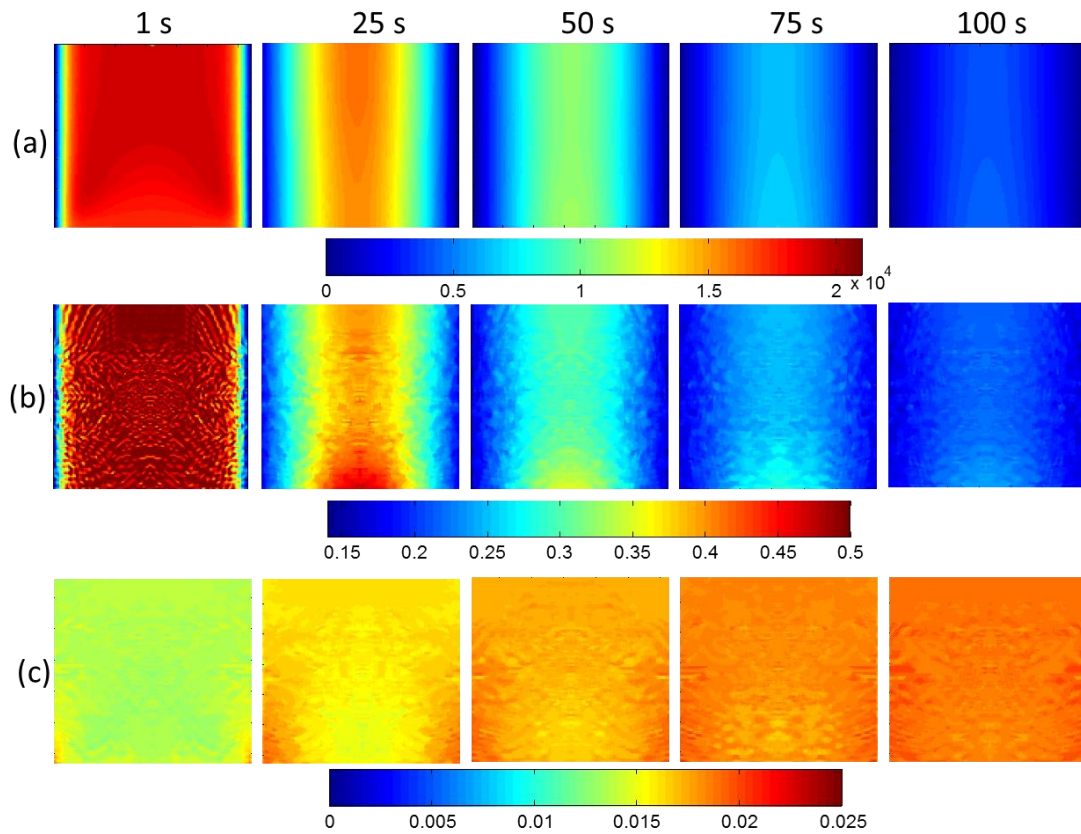
Figure 4.1: Poroelastograms for the homogenous phantom (k= 1.95x10$^{-9}$ m$^4$/N.s) showing the temporal behavior of (a) IFP (b) EPR and (c) Axial strains.

These observations are documented in figure 4.2 which shows the estimated time

constant (TC) of the homogenous phantom for the mean IFP, EPR and axial strain.
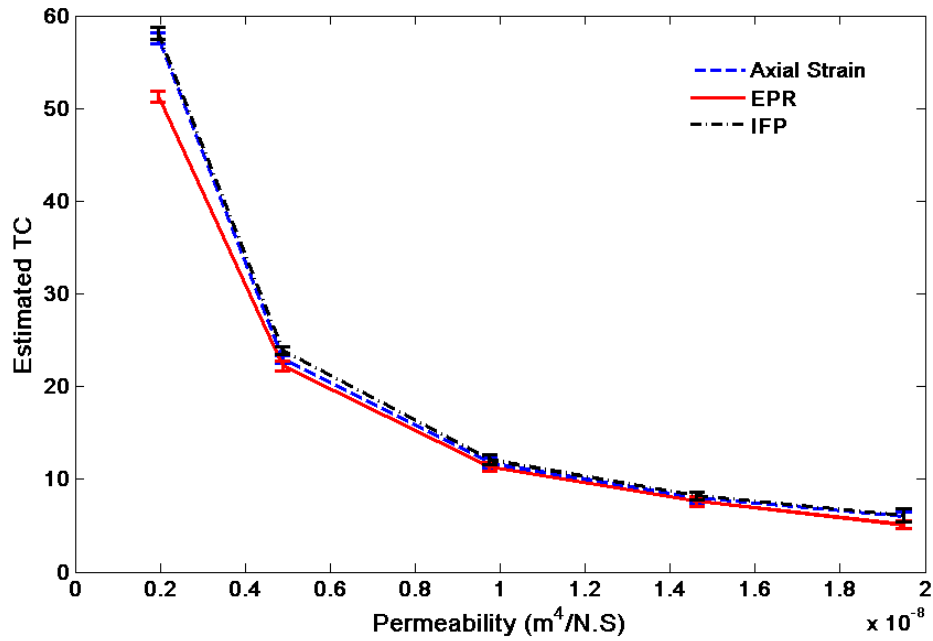
Figure 4.2: Estimated mean TC of the homogenous phantom with variation in underlying permeability.

Figure 4.3 shows the temporal images of IFP, EPR and axial strain for the inclusion

phantom. Due to different interstitial permeability, the inclusion and background exhibit

different temporal behavior. Due to lower permeability, the inclusion takes much longer

to reach its equilibrium value in all three cases- IFP, EPR and axial strain.
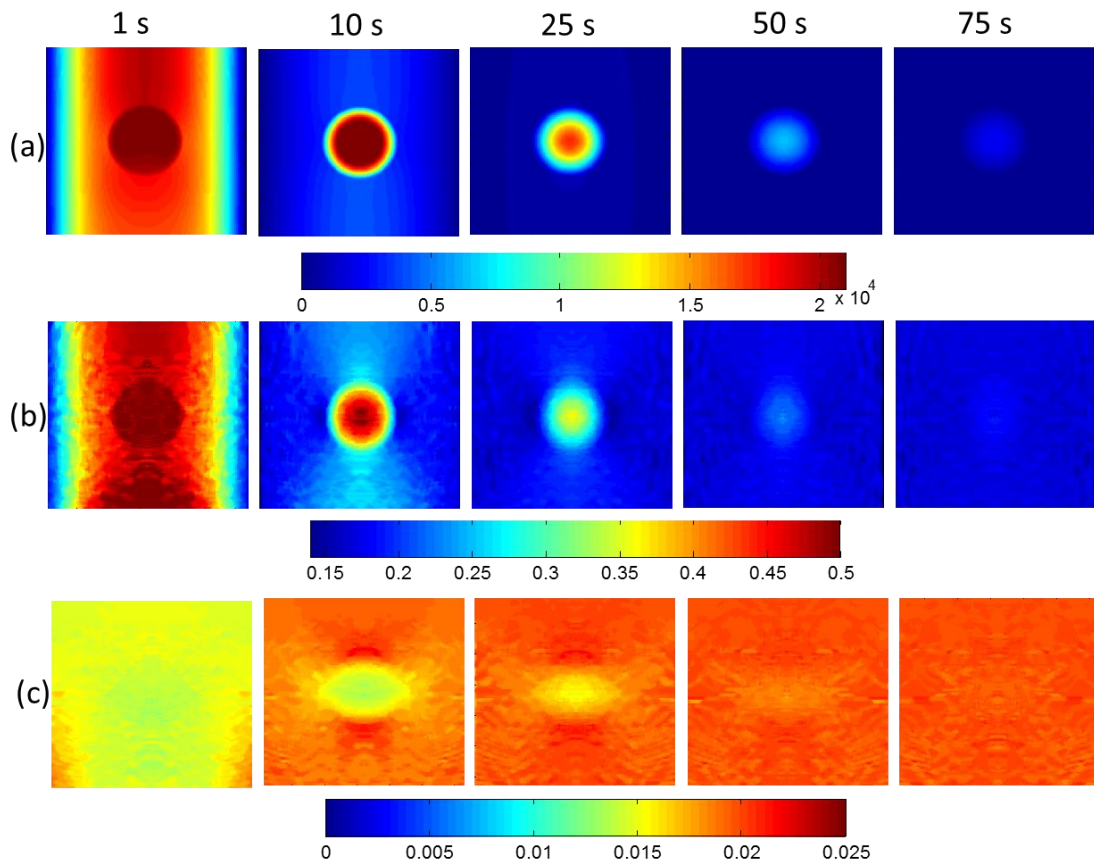
Figure 4.3: Poroelastograms for the inclusion phantom (20 dB) showing the temporal behavior of (a) IFP (b) EPR and (c) Axial strains.

We calculated the mean TC of the inclusion with change in interstitial permeability and the observations are documented in figure 4.4.
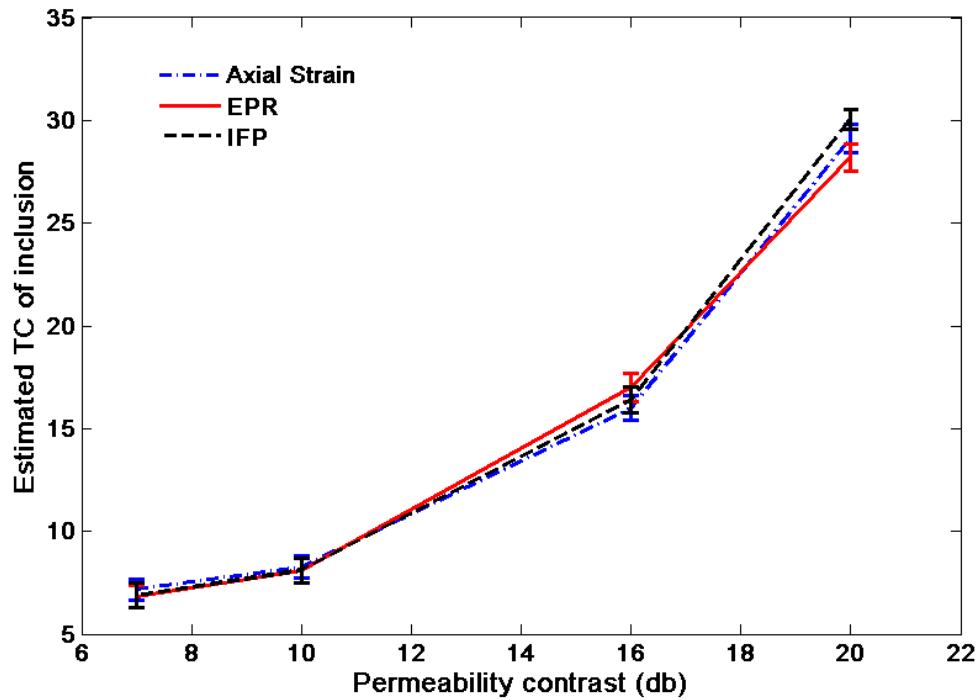
Figure 4.4: Estimated mean TC of the inclusion for the non-homogeous phantom with given underlying permeability contrast.

Figure 4.5 and 4.6 show the time constant images for IFP, EPR and axial strain for the homogenous and inclusion phantoms respectively. It can be observed that the image of the EPR closely resembles that of the IFP.
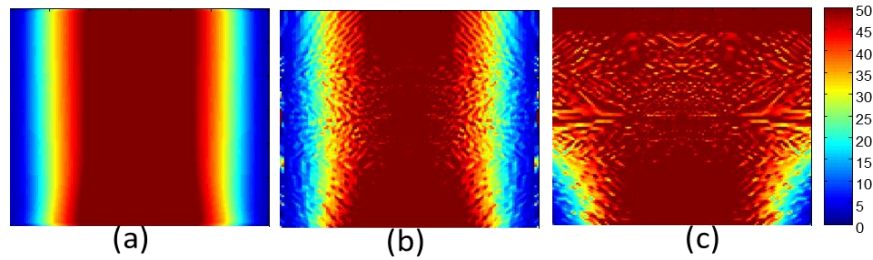
Figure 4.5: Time constant images for the homogeous phantom for (a) IFP (b) EPR (c) axial strain.

## Discussion

For a poroelastic material under uni-axial compression the temporal behavior of the axial and lateral strains is mathematically dependent on the underlying pressure fields(Armstrong, et al. 1984). Under uniaxial loading three temporal stages can be observed: 1) instantaneously after loading, the material behaves like an incompressible solid. The stress is fully supported by the fluid phase, which increases the pore pressure; 2) the stress is then partially transferred to the solid matrix, and fluid begins to exude causing a decrease in volume and EPR. During this transition time, the pore pressure also decays as the solid matrix deforms both in the axial and lateral directions 3) when the equilibrium condition is reached, fluid flow ceases and the pore pressure drops to zero. The rates at which the axial strain and EPR reach their equilibrium value depend upon the ease at which the interstitial fluid flows which in turn depends upon the relaxation of the underlying pressure fields(Leiderman, et al. 2006).

Figure 4.6: Time constant images for the inclusion phantom for (a) IFP (b) EPR (c) axial strain.

Figure 4.1 shows the temporal images obtained from the homogenous phantom for all three parameters analyzed in this study- IFP, EPR and axial strain respectively. Immediately after the compression the fluid pressure increases, the applied load is sustained by the solid matrix and the phantom expands in the lateral direction without losing volume. Hence the EPR of the image is close to 0.5. After this instance pressure relaxation takes place due to established pressure gradient between the compressed material and the boundary(Armstrong, et al. 1984). Since the top and bottom boundaries are confined fluid exudation starts to take place through the sides. The flow of interstitial fluid causes loss in volume along with creating spatio-temporal patterns in both the EPR and axial strain images. The loss of volume due to exudation of fluid causes the EPR to decrease from 0.5 and it exponentially decreases to its equilibrium. It can be observed that the pressure and EPR in the center of the phantom take more time to reach equilibrium than the sides. This is because fluid from the center of the phantom

takes more time to reach the boundary (Armstrong, et al. 1984). Similarly the axial

strains increase to its equilibrium value as the pressure relaxes due to interstitial fluid

flow. These results are similar to that obtained in (Leiderman, et al. 2006). Figure 4.2

shows the estimated time constant of the mean of the image. The graph shows that the

average rate of change of IFP, EPR and axial strains have a non-linear relationship to the

underlying permeability. The estimated TC decrease drastically between the first two

steps and can be noticed to plateau as the permeability is increased further.

Figure 4.3 shows the temporal images of IFP, EPR and axial strain for the inclusion

phantom.  It can be observed that an elevated IFP creates a new contrast mechanism in

both the EPR and axial strain images without an underlying contrast in the elastic

modulus. Due to difference in interstitial permeability, both the background and the

inclusion have different temporal behaviors. The inclusion takes much longer to reach its

equilibrium value for IFP, EPR and axial strain due to slower flow of interstitial fluid.

Figure 4.4 shows the estimated time constants of the inclusion with varying interstitial

permeability. TC increases with increasing contrast i.e. with decrease in permeability in

a non-linear way. Similar to the homogenous case there is a close relationship between

the temporal behavior of the IFP, EPR and axial strain images.

In this study we compare the local and temporal behavior of IFP with that of axial strain

and EPR. The poroelastograms and estimated TC of the mean curves show that the

temporal behavior of IFP is closely related to axial strain and EPR on a global scale.

Overall the pressure gradients created due to the applied load and the resulting pressure

relaxation due to interstitial fluid flow cause the temporal behavior in the axial strain and

EPR poroelastograms. As the pressure approaches zero the mean axial strain and EPR reach their equilibrium values. However it can be observed from figures 4.1 and 5 that the local spatio-temporal patterns of the IFP are similar to that of the EPR and do not resemble that of the axial strains. This may be due to the fact that after compression, the solid matrix recoils and the fluid flows from the sides in the lateral direction causing more significant changes in the lateral strain. Also most of the local changes caused due to the pressure relaxation and the resulting fluid flow result in a change of volume which is more accurately represented in the EPR images. This indicates that EPR may be used to non-invasively estimate the underlying behavior of IFP, which is an important parameter when it comes to soft-tissue cancers and therapy. Traditionally invasive methods have been used to estimate IFP. Other than the fact that they are invasive, their efficiency is also limited because they provide pressure values at a point rather than a map, which might give more diagnostic information.

## Conclusion

In this study we show that interstitial permeability of the material affects the relaxation time of the interstitial fluid pressure in a non-linear fashion. Also, the spatio-temporal behavior of IFP is closely related to that of EPR and estimation of EPR using poroelastography techniques may aid in non-invasive assessment of IFP.

# 5. CONCLUSION

In this section I briefly summarize the work presented in this dissertation. I also discuss some of the future projects that can be envisioned as a result of the conclusions observed through this work.

## Summary

In this dissertation I attempted to address a few of the current major problems in the field of ultrasound poroelastography. Section 2 describes a new class of phantoms that can be used for poroelastography experiments. One of the biggest challenges in poroelastography has been the lack of controlled phantoms that can be used to validate/ predict the results of simulations and experiments. Until now tofu has been the only choice. However, being a commercial product tofu does not come with known mechanical parameters. Also the fluid flow and poroelastic properties of tofu cannot be altered. In this work I developed a first of its kind controlled and tunable tissue mimicking phantom for poroelastography studies. Results indicate that using polyacrylamide gel tissue mimicking phantoms with controlled pore size and fluid mobility can be created. The phantom could be of great use to all the labs in the world conducting research in the field of poroelasticity imaging and temporal elastography imaging in general, hence helping in moving the field forward.

In poroelastography, the EPR image is obtained as the ratio between the lateral strain elastogram and the corresponding axial strain elastogram. Underlying fluid flow mechanisms cause a change in the spatial and temporal behavior of EPR, which is an important parameter because it is related to true changes in volume of the material due to

fluid flow rather than viscoelastic changes. The image quality of EPR elastogram is limited by of the poor quality of standard lateral strain elastography. In section 4 I investigated a new technique to estimate EPR in non-homogenous porous media using two transducers. The feasibility of the technique was tested using finite-element analysis and experimental validation. The results of the study suggest that using this technique it is may be feasible to estimate the temporal behavior of poroelastographic EPR with good image quality while minimizing errors. The experimental implementation in its current form has some limitations which warrant further investigation.

Interstitial fluid pressure (IFP) is an important parameter relevant to soft tissue cancers. Most soft tissue cancers are known to show elevated IFP and altered interstitial permeability. In section 4 I investigated the effect of interstitial permeability on the spatio-temporal behavior of the underlying fluid pressure field. I also investigated the relationship between the temporal behavior of estimated poroelastography parameters such as axial strain and effective Poisson's ratio (EPR) and IFP. Results of the study indicate the following - increased IFP creates a new contrast mechanism in the axial strain and EPR elastograms, the temporal behavior of IFP changes non-linearly with underlying interstitial permeability and the spatio-temporal patterns of IFP are closely related to that of the EPR.

**Future work**

**Creation and analysis of complex poroelastic phantoms with applications in lymphedema and cancer imaging**

In section 2 we describe a new phantom material for poroelastography studies. We show that by using polyacrylamide gel new type of tissue mimicking phantoms with controlled pore size and fluid flow can be created. We investigated the use of the new material to create two kinds of phantoms- homogenous and one with a single inclusion in the center. The same material can be used to create more complex phantoms. For e.g. poroelastography has been shown to successfully diagnose and stage lymphedema (Raffaella, et al. 2007) which has been previously modeled in finite element simulations as a bi-layer media (Chaudhry 2010). Some of the results obtained from previous in-vivo and FEA studies can be validated by creating a bi-layer phantom using this new phantom material developed in this study. Figure 5.1 shows the schematic of the proposed phantom.
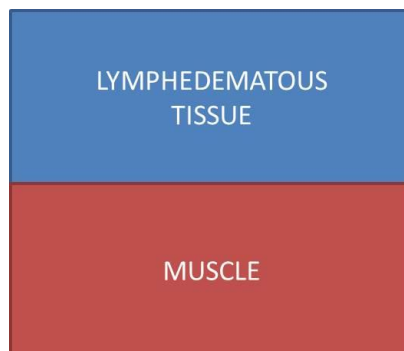


Figure 5.1: Schematic for bi-layer phantom mimicking lymphedema condition.

The same phantom material can also be used to create complex tumor models. In many cases, especially malignant cancers, more than one instance of a tumor can be found. Such complex cases can also be simulated using polyacrylamide gel. The boundary conditions of the two tumors in the presence of each other may create new spatio-temporal patterns in the axial strain images. Figure 5.2 shows the schematic of the proposed multi-tumor phantom.
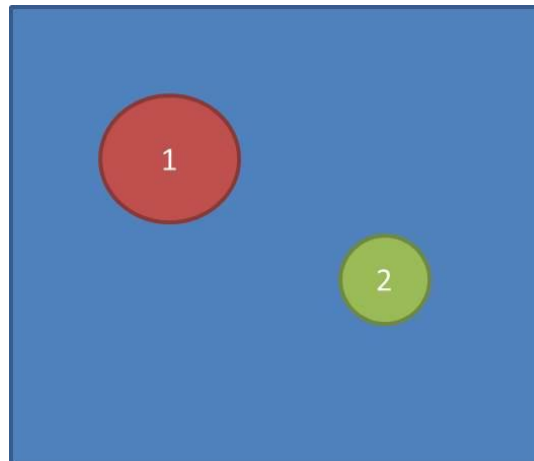


Figure 5.2: Schematic of proposed multi-tumor phantom.

**An automated system for efficient imaging of EPR poroelastograms**

In section 3 we demonstrated the feasibility of using two ultrasound transducers to estimate the effective Poisson's ratio (EPR) in poroelastic media. The simulations showed that the two transducer method had superior performance than the previously used techniques. Although the study showed the usefulness of using two ultrasound

transducers instead of one, the experimental setup in its current form has some limitations. Due to the positioning of the transducers and the size of the compressor plate, samples with only specific sizes and geometries can be imaged. A two transducer system implemented on two C-arms making 45 degrees angle with the horizontal will solve some of these issues.  Also a controlled compressor system with calibrated motion will simplify the manual calibration and registration modules.  The current Ultrasonix system we used had the capability of using two transducers as an input, however switching between them is done by a mechanical relay switch.  For this reason we had to use two separate systems each for axial and lateral data acquisition. In future if the switching between the transducers could be controlled by an electronic switch, a single system can be successfully used. These engineering improvements will make the technique more suitable for ex-vivo and clinical application. Figure 5.3 shows the schematic of the proposed two transducer system with recommended improvements.
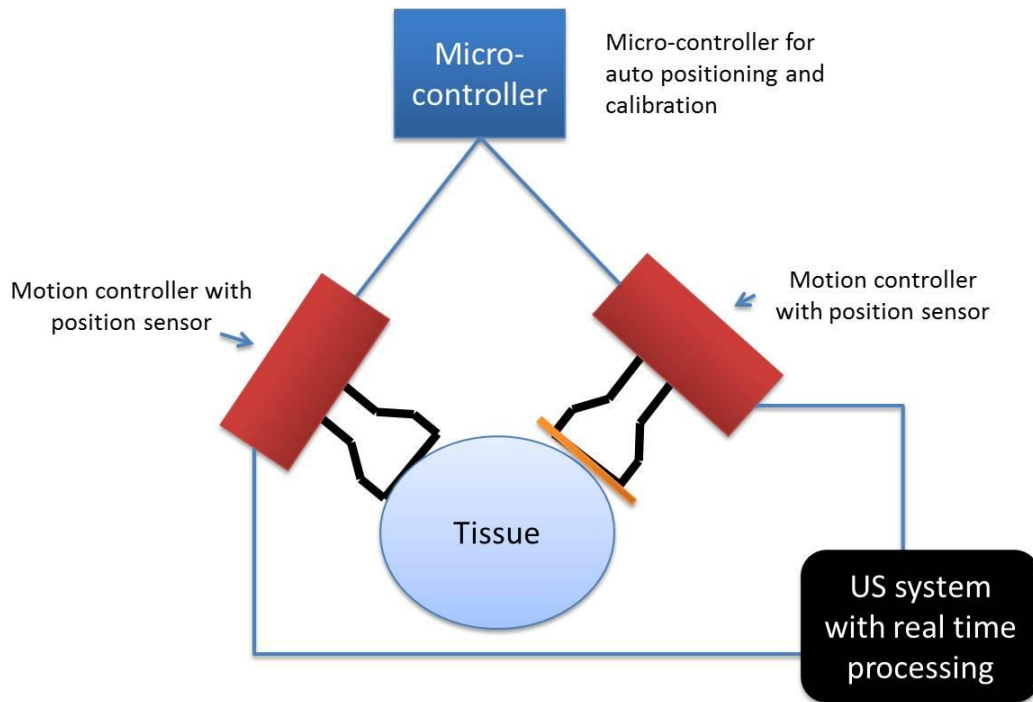
Figure 5.3: Schematic of proposed improvements to the two transducer ultrasound system.

**Effect of elevated IFP on the axial strain poroelastography**

In this dissertation, we also investigated the effect of interstitial fluid flow on the temporal behavior of interstitial fluid pressure (IFP). The study also shows that the spatio-temporal behavior of IFP is very closely related to that of the EPR and investigation of EPR may aid in non-invasive assessment of IFP. I also attempted to investigate the effect of elevated IFP on the spatio-temporal behavior of axial strain and EPR using finite element analysis (FEA).  Figure 5.4 shows the quasi-static axial strain images of increasing simulated IFP. The pressure in the background was maintained at 0 mmHg. It can be observed that elevated IFP creates a contrast in the corresponding axial

strain images. The contrast can also be seen to increase as the IFP is increased between 5 and 35 mmHg.
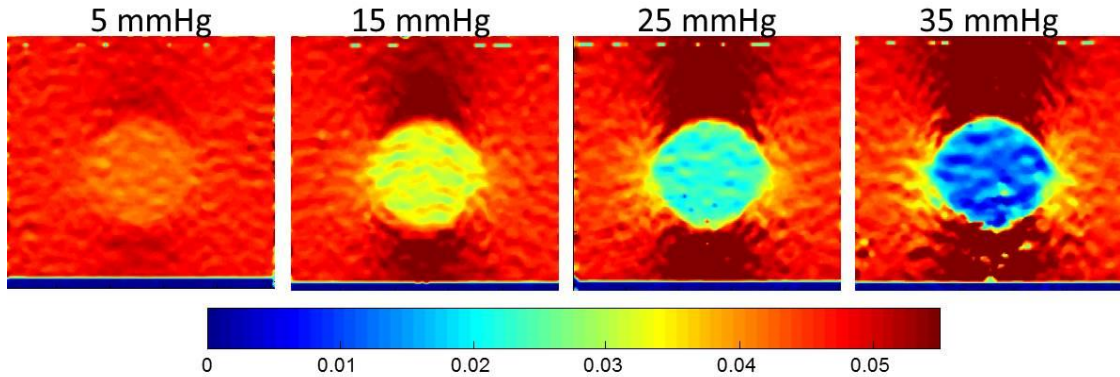


Figure 5.4: Quasi-static axial strain images of increasing simulated IFP

We could not analyze the temporal behavior of axial strains as the FEA implementation of the tumor model did not converge in ABAQUS for time t>0 s. In future the transient analysis can be conducted using an in-house software created using analytical solutions similar to that used in (Chaudhry, et al. 2013). Understanding the effect of elevated IFP on temporal elastography studies will help in better understanding of in-vivo results especially in cases of tumors where IFP is known to be high.

# REFERENCES

Abbott NJ. Evidence for bulk flow of brain interstitial fluid: significance for physiology and pathology. Neurochemistry international 2004; 45:545-52.

Abeysekera JM, Zahiri Azar R, Goksel O, Rohling R, Salcudean SE. Analysis of 2-D motion tracking in ultrasound with dual transducers. Ultrasonics 2012; 52:156-68.

Armstrong C, Lai W, Mow V. An analysis of the unconfined compression of articular cartilage. Journal of biomechanical engineering 1984; 106:165-73.

Bamber J, Hill C. Ultrasonic attenuation and propagation speed in mammalian tissues as a function of temperature. Ultrasound in medicine & biology 1979; 5:149-57.

Bamber JC. Acoustical characteristics of biological media. Encyclopedia of Acoustics, Volume Four 2007:1703-26.

Baselga J, Hernandez-Fuentes I, Pierola I, Llorente M. Elastic properties of highly crosslinked polyacrylamide gels. Macromolecules 1987; 20:3060-65.

Bercoff J, Tanter M, Fink M. Supersonic shear imaging: a new technique for soft tissue elasticity mapping. Ultrasonics, Ferroelectrics and Frequency Control, IEEE Transactions on 2004; 51:396-409.

Berry GP, Bamber JC, Armstrong CG, Miller NR, Barbone PE. Towards an acoustic model-based poroelastic imaging method: I. Theoretical foundation. Ultrasound Med Biol 2006; 32:547-67.

Berry GP, Bamber JC, Miller NR, Barbone PE, Bush NL, Armstrong CG. Towards an acoustic model-based poroelastic imaging method: II. experimental investigation. Ultrasound Med Biol 2006; 32:1869-85.

Biot M. Le problème de la consolidation des matières argileuses sous une charge. Ann. Soc. Sci. Bruxelles B 1935; 55:110-13.

Biot MA. General theory of three-dimensional consolidation. Journal of applied physics 1941; 12:155-64.

Blattler D, Garner F, Van Slyke K, Bradley A. Quantitative electrophoresis in polyacrylamide gels of 2–40%. Journal of Chromatography A 1972; 64:147-55.

Boucher Y, Baxter LT, Jain RK. Interstitial pressure gradients in tissue-isolated and subcutaneous tumors: implications for therapy. Cancer research 1990; 50:4478-84.

Boucher Y, Kirkwood JM, Opacic D, Desantis M, Jain RK. Interstitial hypertension in superficial metastatic melanomas in humans. Cancer research 1991; 51:6691-94.

Boucher Y, Salehi H, Witwer B, Harsh G. Interstitial fluid pressure in intracranial tumours in patients and in rodents. British journal of cancer 1997; 75:829.

Boudou T, Ohayon J, Picart C, Tracqui P. An extended relationship for the characterization of Young's modulus and Poisson's ratio of tunable polyacrylamide gels. Biorheology 2006; 43:721-8.

Bu-Lin Z, Bing H, Sheng-Li K, Huang Y, Rong W, Jia L. A polyacrylamide gel phantom for radiofrequency ablation. International Journal of Hyperthermia 2008; 24:568-76.

Caulfield MJ, Hao X, Qiao GG, Solomon DH. Degradation on polyacrylamides. Part II. Polyacrylamide gels. Polymer 2003; 44:3817-26.

Cespedes I, Ophir J, Ponnekanti H, Maklad N. Elastography: Elasticity Imaging Using Ultrasound with Application to Muscle and Breast< i> In Vivo</i>. Ultrasonic imaging 1993; 15:73-88.

Chaudhry A. 2010 Effect of boundary condition on performance of poroelastographic imaging techniques in non homogeous poroelastic media: Texas A&M University.

Chaudhry A, Unnikrishnan G, Reddy J, Krouskop TA, Righetti R. Effect of Permeability on the Performance of Elastographic Imaging Techniques. Medical Imaging, IEEE Transactions on 2013; 32:189-99.

Choi MJ, Guntur SR, Lee KI, Paeng DG, Coleman A. A tissue mimicking polyacrylamide hydrogel phantom for visualizing thermal lesions generated by high intensity focused ultrasound. Ultrasound in medicine & biology 2013; 39:439-48.

Chrambach A, Rodbard D. Polyacrylamide gel electrophoresis. Science 1971; 172:440-51.

Culjat MO, Goldenberg D, Tewari P, Singh RS. A review of tissue substitutes for ultrasound imaging. Ultrasound in medicine & biology 2010; 36:861-73.

Detournay E, Cheng AH-D. Fundamentals of Poroelasticity1. 1993.

Doyley MM. Model-based elastography: a survey of approaches to the inverse elasticity problem. Physics in Medicine and Biology 2012; 57:R35.

Duck FA. Physical properties of tissues: a comprehensive reference book: Academic press, 2013.

Fadnes HO, Reed RK, Aukland K. Interstitial fluid pressure in rats measured with a modified wick technique. Microvascular research 1977; 14:27-36.

Fatt I. Dynamics of water transport in the corneal stroma. Experimental eye research 1968; 7:402-12.

Frenkel V, Etherington A, Greene M, Quijano J, Xie J, Hunter F, Dromi S, Li KC. Delivery of liposomal doxorubicin (Doxil) in a breast cancer tumor model: investigation of potential enhancement by pulsed-high intensity focused ultrasound exposure. Academic radiology 2006; 13:469-79.

Galli M, Comley KSC, Shean TAV, Oyen ML. Viscoelastic and poroelastic mechanical characterization of hydrated gels. Journal of Materials Research 2009; 24:973-79.

Gao L, Parker K, Lerner R, Levinson S. Imaging of the elastic properties of tissue—A review. Ultrasound in medicine & biology 1996; 22:959-77.

Ginat DT, Destounis SV, Barr RG, Castaneda B, Strang JG, Rubens DJ. US elastography of breast and prostate lesions 1. Radiographics 2009; 29:2007-16.

Griffon-Etienne G, Boucher Y, Brekken C, Suit HD, Jain RK. Taxane-induced apoptosis decompresses blood vessels and lowers interstitial fluid pressure in solid tumors clinical implications. Cancer research 1999; 59:3776-82.

Gutmann R, Leunig M, Feyh J, Goetz AE, Messmer K, Kastenbauer E, Jain RK. Interstitial hypertension in head and neck tumors in patients: correlation with tumor size. Cancer research 1992; 52:1993-95.

Hall TJ, Bilgen M, Insana MF, Krouskop TA. Phantom materials for elastography. Ultrasonics, Ferroelectrics, and Frequency Control, IEEE Transactions on 1997; 44:1355-65.

Hall TJ, Bilgen M, Insana MF, Krouskop TA. Phantom materials for elastography. Ultrasonics, Ferroelectrics and Frequency Control, IEEE Transactions on 1997; 44:1355-65.

Hassid Y, Furman-Haran E, Margalit R, Eilam R, Degani H. Noninvasive magnetic resonance imaging of transport and interstitial fluid pressure in ectopic human lung tumors. Cancer research 2006; 66:4159-66.

Heldin C-H, Rubin K, Pietras K, Östman A. High interstitial fluid pressure—an obstacle in cancer therapy. Nature Reviews Cancer 2004; 4:806-13.

Hiltawsky KM, Krüger M, Starke C, Heuser L, Ermert H, Jensen A. Freehand ultrasound elastography of breast lesions: clinical results. Ultrasound in medicine & biology 2001; 27:1461-69.

Holmes DL, Stellwagen NC. Estimation of polyacrylamide gel pore size from Ferguson plots of linear DNA fragments. II. Comparison of gels with different crosslinker concentrations, added agarose and added linear polyacrylamide. Electrophoresis 1991; 12:612-19.

Hompland T, Ellingsen C, Øvrebø KM, Rofstad EK. Interstitial fluid pressure and associated lymph node metastasis revealed in tumors by dynamic contrast-enhanced MRI. Cancer research 2012; 72:4899-908.

Itoh A, Ueno E, Tohno E, Kamma H, Takahashi H, Shiina T, Yamakawa M, Matsumura T. Breast disease: Clinical application of us elastography for diagnosis 1. Radiology 2006; 239:341-50.

Jain RK. Transport of molecules in the tumor interstitium: a review. Cancer Res 1987; 47:3039-51.

Jain RK. Barriers to drug delivery in solid tumors. Scientific American 1994:58-65.

Jurvelin J, Buschmann M, Hunziker E. Optical and mechanical determination of Poisson's ratio of adult bovine humeral articular cartilage. Journal of biomechanics 1997; 30:235-41.

Kalcioglu ZI, Mahmoodian R, Hu Y, Suo Z, Van Vliet KJ. From macro-to microscale poroelastic characterization of polymeric hydrogels via indentation. Soft Matter 2012; 8:3393-98.

Kallel F, Bertrand M. Tissue elasticity reconstruction using linear perturbation method. Medical Imaging, IEEE Transactions on 1996; 15:299-313.

Kallel F, Bertrand M, Ophir J. Fundamental limitations on the contrast-transfer efficiency in elastography: an analytic study. Ultrasound in medicine & biology 1996; 22:463-70.

Kallel F, Prihoda CD, Ophir J. Contrast-transfer efficiency for continuously varying tissue moduli: Simulation and phantom validation. Ultrasound in medicine & biology 2001; 27:1115-25.

Kallel F, Varghese T, Ophir J, Bilgen M. The nonstationary strain filter in elastography: Part II. lateral and elevational decorrelation. Ultrasound in medicine & biology 1997; 23:1357-69.

Kawabata K-i, Waki Y, Matsumura T, Umemura S-i. 2004 Tissue mimicking phantom for ultrasonic elastography with finely adjustable elastic and echographic properties. Ultrasonics Symposium, 2004 IEEE: IEEE, 1502-05.

Kharine A, Manohar S, Seeton R, Kolkman RG, Bolt RA, Steenbergen W, de Mul FF. Poly (vinyl alcohol) gels for use as tissue phantoms in photoacoustic mammography. Physics in medicine and biology 2003; 48:357.

Konofagou E, Ophir J. A new elastographic method for estimation and imaging of lateral displacements, lateral strains, corrected axial strains and Poisson's ratios in tissues. Ultrasound in medicine & biology 1998; 24:1183-99.

Konofagou EE, Harrigan TP, Ophir J, Krouskop TA. Poroelastography: imaging the poroelastic properties of tissues. Ultrasound Med Biol 2001; 27:1387-97.

Konofagou EE, Harrigan TP, Ophir J, Krouskop TA. Poroelastography: imaging the poroelastic properties of tissues. Ultrasound in medicine & biology 2001; 27:1387-97.

Kristjansen PE, Boucher Y, Jain RK. Dexamethasone reduces the interstitial fluid pressure in a human colon adenocarcinoma xenograft. Cancer research 1993; 53:4764-66.

Lafon C, Kaczkowski PJ, Vaezy S, Noble M, Sapozhnikov O. 2001 Development and characterization of an innovative synthetic tissue-mimicking material for high intensity focused ultrasound (HIFU) exposures. Ultrasonics Symposium, 2001 IEEE: IEEE, 1295-98.

Lamdan Y, Schwartz JT, Wolfson HJ. 1988 Object recognition by affine invariant matching. Computer Vision and Pattern Recognition, 1988. Proceedings CVPR'88., Computer Society Conference on: IEEE, 335-44.

Leiderman R, Barbone PE, Oberai AA, Bamber JC. Coupling between elastic strain and interstitial fluid flow: ramifications for poroelastic imaging. Phys Med Biol 2006; 51:6291-313.

Leunig M, Yuan F, Menger MD, Boucher Y, Goetz AE, Messmer K, Jain RK. Angiogenesis, microvascular architecture, microhemodynamics, and interstitial fluid pressure during early growth of human adenocarcinoma LS174T in SCID mice. Cancer Research 1992; 52:6553-60.

Li C, Allen J, Alliston T, Pruitt LA. The use of polyacrylamide gels for mechanical calibration of cartilage—A combined nanoindentation and unconfined compression study. Journal of the mechanical behavior of biomedical materials 2011; 4:1540-47.

Lorenz A, Ermert H, Sommerfeld H, Garcia-Schürmann M, Senge T, Philippou S. [Ultrasound elastography of the prostate. A new technique for tumor detection]. Ultraschall in der Medizin (Stuttgart, Germany: 1980) 2000; 21:8-15.

Lubinski MA, Emelianov SY, Raghavan K, Yagle AE, Skovoroda AR, O'Donnell M. Lateral displacement estimation using tissue incompressibility. IEEE Transactions on Ultrasonics Ferroelectrics and Frequency Control 1996; 43:247-56.

Lunt SJ, Fyles A, Hill RP, Milosevic M. Interstitial fluid pressure in tumors: therapeutic barrier and biomarker of angiogenesis. 2008.

Madsen EL, Frank GR. 1999 Method of making a solid tissue mimicking material for ultrasound phantoms: Google Patents.

Madsen EL, Hobson MA, Shi H, Varghese T, Frank GR. Tissue-mimicking agar/gelatin materials for use in heterogeneous elastography phantoms. Physics in medicine and biology 2005; 50:5597.

Milosevic M, Fyles A, Hedley D, Pintilie M, Levin W, Manchul L, Hill R. Interstitial fluid pressure predicts survival in patients with cervix cancer independent of clinical prognostic factors and tumor oxygen measurements. Cancer research 2001; 61:6400-05.

Milosevic M, Lunt SJ, Leung E, Skliarenko J, Shaw P, Fyles A, Hill RP. Interstitial permeability and elasticity in human cervix cancer. Microvascular research 2008; 75:381-90.

Mow VC, Holmes MH, Michael Lai W. Fluid transport and mechanical properties of articular cartilage: a review. Journal of biomechanics 1984; 17:377-94.

Mridha M, Odman S. Noninvasive method for the assessment of subcutaneous oedema. Medical & biological engineering & computing 1986; 24:393-8.

Murphy MB, Khaled S, Fan D, Yazdi IK, Sprintz M, Buchanan RM, Smid CA, Weiner BK, Ferrari M, Tasciotti E. A multifunctional nanostructured platform for localized sustained release of analgesics and antibiotics. European Journal of Pain Supplements 2011; 5:423-32.

Nair S, Righetti R. Resimulation of noise: a precision estimator for least square error curve-fitting tested for axial strain time constant imaging. Physics in medicine and biology 2015; 60:3515.

Nair S, Varghese J, Chaudhry A, Righetti R. Effect of Temporal Acquisition Parameters on Image Quality of Strain Time Constant Elastography. Ultrasonic Imaging 2014.

Nair SP, Xu Y, Krouskop TA, Righetti R. Performance Analysis of a New Real-Time Elastographic Time Constant Estimator. Medical Imaging, IEEE Transactions on 2011; 30:497-511.

Nathanson SD, Nelson L. Interstitial fluid pressure in breast cancer, benign breast conditions, and breast parenchyma. Annals of surgical oncology 1994; 1:333-38.

Netti PA, Baxter LT, Boucher Y, Skalak R, Jain RK. Time-dependent behavior of interstitial fluid pressure in solid tumors: implications for drug delivery. Cancer Research 1995; 55:5451-58.

Netti PA, Berk DA, Swartz MA, Grodzinsky AJ, Jain RK. Role of extracellular matrix assembly in interstitial transport in solid tumors. Cancer research 2000; 60:2497-503.

Nightingale KR, Palmeri ML, Nightingale RW, Trahey GE. On the feasibility of remote palpation using acoustic radiation force. The Journal of the Acoustical Society of America 2001; 110:625-34.

Ophir J, Alam SK, Garra B, Kallel F, Konofagou E, Krouskop T, Varghese T. Elastography: Ultrasonic estimation and imaging of the elastic properties of tissues. Proceedings of the Institution of Mechanical Engineers, Part H: Journal of Engineering in Medicine 1999; 213:203-33.

Ophir J, Cespedes I, Garra B, Ponnekanti H, Huang Y, Maklad N. Elastography: ultrasonic imaging of tissue strain and elastic modulus in vivo. European journal of ultrasound 1996; 3:49-70.

Ophir J, Cespedes I, Ponnekanti H, Yazdi Y, Li X. Elastography: a quantitative method for imaging the elasticity of biological tissues. Ultrasonic imaging 1991; 13:111-34.

Ophir J, Cespedes I, Ponnekanti H, Yazdi Y, Li X. Elastography: a quantitative method for imaging the elasticity of biological tissues. Ultrason Imaging 1991; 13:111-34.

Ozerdem U, Hargens AR. A simple method for measuring interstitial fluid pressure in cancer tissues. Microvascular research 2005; 70:116-20.

Ozsun O, Thompson RL, Ekinci KL, Tien J. Non-invasive mapping of interstitial fluid pressure in microscale tissues. Integrative Biology 2014; 6:979-87.

Park JW. Liposome-based drug delivery in breast cancer treatment. Breast Cancer Research 2002; 4:95.

Petrek JA, Senie RT, Peters M, Rosen PP. Lymphedema in a cohort of breast carcinoma survivors 20 years after diagnosis. Cancer 2001; 92:1368-77.

Ponnekanti H, Ophir J, Huang Y, Cespedes I. Fundamental mechanical limitations on the visualization of elasticity contrast in elastography. Ultrasound Med Biol 1995; 21:533-43.

Prokop AF, Vaezy S, Noble ML, Kaczkowski PJ, Martin RW, Crum LA. Polyacrylamide gel as an acoustic coupling medium for focused ultrasound therapy. Ultrasound in medicine & biology 2003; 29:1351-58.

Qiu Y, Sridhar M, Tsou JK, Lindfors KK, Insana MF. Ultrasonic viscoelasticity imaging of nonpalpable breast tumors: preliminary results. Academic radiology 2008; 15:1526-33.

Raffaella R, Brian SG, Louise MM, Christina MK-C, Jonathan O, Thomas AK. The feasibility of using poroelastographic techniques for distinguishing between normal and lymphedematous tissues in vivo. Physics in Medicine and Biology 2007; 52:6525.

Raffaella R, Seshadri S, Arun Thitai K, Jonathan O, Thomas AK. Assessing image quality in effective Poisson's ratio elastography and poroelastography: I. Physics in Medicine and Biology 2007; 52:1303.
Raymond S, Wang Y-J. Preparation and properties of acrylamide gel for use in electrophoresis. Analytical biochemistry 1960; 1:391-96.

Righetti R, Chaudhry A, Nair S. 2011 Fundamental image quality parameters of poroelastography. Biomedical Imaging: From Nano to Macro, 2011 IEEE International Symposium on: IEEE, 1614-17.

Righetti R, Ophir J, Garra BS, Chandrasekhar RM, Krouskop TA. A new method for generating poroelastograms in noisy environments. Ultrasonic imaging 2005; 27:201-20.

Righetti R, Ophir J, Krouskop TA. A method for generating permeability elastograms and Poisson's ratio time-constant elastograms. Ultrasound in medicine & biology 2005; 31:803-16.

Righetti R, Ophir J, Kumar AT, Krouskop TA. Assessing image quality in effective Poisson's ratio elastography and poroelastography: II. Physics in medicine and biology 2007; 52:1321.

Righetti R, Ophir J, Srinivasan S, Krouskop TA. The feasibility of using elastography for imaging the Poisson's ratio in porous media. Ultrasound in Medicine & Biology 2004; 30:215-28.

Righetti R, Righetti M, Ophir J, Krouskop TA. The feasibility of estimating and imaging the mechanical behavior of poroelastic materials using axial strain elastography. Physics in medicine and biology 2007; 52:3241.

Roh H, Boucher Y, Kalnicki S, Buchsbaum R, Bloomer W, Jain R. Interstitial hypertension in carcinoma of uterine cervix in patients: possible correlation with tumor oxygenation and radiation response. Cancer Research 1991; 51:6695-98.

Sandrin L, Fourquet B, Hasquenoph J-M, Yon S, Fournier C, Mal F, Christidis C, Ziol M, Poulet B, Kazemi F. Transient elastography: a new noninvasive method for assessment of hepatic fibrosis. Ultrasound in medicine & biology 2003; 29:1705-13.

Sarron J-C, Blondeau C, Guillaume A, Osmont D. Identification of linear viscoelastic constitutive models. Journal of biomechanics 2000; 33:685-93.

Sarvazyan A, Hall TJ, Urban MW, Fatemi M, Aglyamov SR, Garra BS. An overview of elastography–an emerging branch of medical imaging. Current medical imaging reviews 2011; 7:255.

Scholander PF, Hargens AR, Miller SL. Negative pressure in the interstitial fluid of animals. Fluid tensions are spectacular in plants; in animals they are elusively small, but just as vital. Science 1968; 161:321-8.

Srinivasan S, Ophir J, Alam S. Elastographic imaging using staggered strain estimates. Ultrasonic Imaging 2002; 24:229-45.

Srinivasan S, Righetti R, Ophir J. Trade-offs between the axial resolution and the signal-to-noise ratio in elastography. Ultrasound in medicine & biology 2003; 29:847-66.

Stapleton S, Milosevic M. Pressure Gradients in Solid Tumors, In: Bae YH, Mrsny RJ, and Park K, eds. Cancer Targeted Drug Delivery: Springer New York, 2013. 241-72.

Stokols S, Tuszynski MH. Freeze-dried agarose scaffolds with uniaxial channels stimulate and guide linear axonal growth following spinal cord injury. Biomaterials 2006; 27:443-51.

Systèmes D. ABAQUS 6.12 Theory manual. Dassault Systèmes Simulia Corp., Providence, Rhode Island 2012.

Szuba A, Rockson S. Lymphedema: anatomy, physiology and pathogenesis. Vascular medicine (London, England) 1997; 2:321-26.

Takegami K, Kaneko Y, Watanabe T, Maruyama T, Matsumoto Y, Nagawa H. Polyacrylamide gel containing egg white as new model for irradiation experiments using focused ultrasound. Ultrasound in medicine & biology 2004; 30:1419-22.

Tang F, Fudouzi H, Uchikoshi T, Sakka Y. Preparation of porous materials with controlled pore size and porosity. Journal of the European Ceramic Society 2004; 24:341-44.

Thitaikumar A, Krouskop TA, Garra BS, Ophir J. Visualization of bonding at an inclusion boundary using axial-shear strain elastography: a feasibility study. Physics in medicine and biology 2007; 52:2615.

Tombs M. The interpretation of gel electrophoresis. Analytical Biochemistry 1965; 13:121-32.

Torzilli P, Mow VC. On the fundamental fluid transport mechanisms through normal and pathological articular cartilage during function—II. The analysis, solution and conclusions. Journal of biomechanics 1976; 9:587-606.

Tse JR, Engler AJ. Preparation of hydrogel substrates with tunable mechanical properties. Current protocols in cell biology 2010:10.16. 1-10.16. 16.

Van Houten EE, Doyley MM, Kennedy FE, Weaver JB, Paulsen KD. Initial in vivo experience with steady-state subzone-based MR elastography of the human breast. Journal of Magnetic Resonance Imaging 2003; 17:72-85.

Varghese T, Ophir J. A theoretical framework for performance characterization of elastography: the strain filter. Ultrasonics, Ferroelectrics and Frequency Control, IEEE Transactions on 1997; 44:164-72.

von Buelow S, von Heimburg D, Pallua N. Efficacy and safety of polyacrylamide hydrogel for facial soft-tissue augmentation. Plastic and reconstructive surgery 2005; 116:1137-46.

Walker-Samuel S, Ramasawmy R, Wells J, Siow B, Johnson S, Pedley R, Lythgoe M. 397 Non-invasive Measurement of Tumour Interstitial Fluid Pressure Using Magnetic Resonance Imaging. european journal of cancer 2012; 48:S96.

Wang HF. Theory of linear poroelasticity. Princeton Series in Geophysics, Princeton University Press, Princeton, NJ 2000.

Watson KD, Lai C-Y, Qin S, Kruse DE, Lin Y-C, Seo JW, Cardiff RD, Mahakian LM, Beegle J, Ingham ES. Ultrasound increases nanoparticle delivery by reducing intratumoral pressure and increasing transport in epithelial and epithelial–mesenchymal transition tumors. Cancer research 2012; 72:1485-93.

White ML. The permeability of an acrylamide polymer gel. The Journal of Physical Chemistry 1960; 64:1563-65.

Wu J. Tofu as a tissue-mimicking material. Ultrasound in medicine & biology 2001; 27:1297-300.

Zakharov SF, Chang HT, Chrambach A. Reproducibility of mobility in gel electrophoresis. Electrophoresis 1996; 17:84-90.

Zell K, Sperl J, Vogel M, Niessner R, Haisch C. Acoustical properties of selected tissue phantom materials for ultrasound imaging. Physics in medicine and biology 2007; 52:N475.

Zhi H, Ou B, Luo B-M, Feng X, Wen Y-L, Yang H-Y. Comparison of ultrasound elastography, mammography, and sonography in the diagnosis of solid breast lesions. Journal of ultrasound in medicine 2007; 26:807-15.